

UNIVERSITÀ DEGLI STUDI DI NAPOLI FEDERICO II



SCUOLA POLITECNICA E DELLE SCIENZE DI BASE

DEPARTMENT OF CHEMICAL, MATERIALS AND
PRODUCTION ENGINEERING (DICMaPI)

PhD Program in “Industrial Product and Process Engineering”

XXXIV cycle

Three-dimensional computational fluid
dynamics simulation of the hollow-cone spray
process

Tutors:

Prof. Pier Luca Maffettone

Ph.D. Deepak Ahirwal

Candidate:

Massimiliano Di Martino

November 2018-November 2021

ABSTRACT

The characterization of atomization in small-scale applications, such as those typical of consumer goods industry, is not widely investigated, despite of its enormous interest as in the case of sanitation. In this field, the features of the atomizer are selected to achieve a wide spray pattern. This is the case of the pressure-swirl atomizer, where the swirl flow leads the liquid sheet to exhibit a distinctive hollow-cone shape. The configuration of the atomizer and the properties of the multiphase system (liquid-gas) affect the spray morphology and the droplets/ligaments distribution.

Aim of the work is to investigate through CFD the stability of the gas-liquid interface produced by a swirling liquid injection at short and long distances from the nozzle outlet. By implementing the VOF and the VOF-to-DPM methods, we show transient simulations in which the liquid-gas interactions and the further propagation of droplets are resolved within and outside the nozzle, simultaneously.

Depending on the different liquid properties and geometric features, we examine the hollow-cone spray performance in terms of cone angle and liquid sheet morphology. A stability analysis allows to determine whether spraying or jetting conditions are attained depending on Reynolds and Ohnesorge numbers, as the hollow-cone shape can degenerate into a straight jet under specific operating conditions.

Viscosity is known to be a relevant parameter in fluid formulation, which impacts on both relevant dimensionless parameters. Newtonian and non-Newtonian rheologies are here considered for their

ubiquitous presence in detergent or sanitation fluids. In both cases, we find a critical condition that marks the switch from spraying to jetting regime. We highlight the relevance of the non-Newtonian liquid properties in the primary atomization of hollow-cone sprays. By increasing the consistency index as well as the shear thinning index, both the liquid sheet sharpness and the aerodynamic interactions on the liquid-gas interface affect the spray performance.

The static mesh refinement allows us to track the liquid-gas interface displacement at small distance from the exit orifice. Subsequently, a dynamic mesh adaption is implemented to improve the mesh quality and capture accurately the primary breakup at longer distance from the nozzle exit orifice. In this way, we compare the Newtonian and non-Newtonian primary atomization also in terms of spray pattern and droplet size distribution from the nozzle outlet to a wall placed further from the primary breakup region.

Index

1. Introduction	1
2. State of art	4
3. Mathematical model and simulation setup.....	12
3.1 Multiphase Volume Of Fluid (VOF) interface capturing method... 15	
3.2 Multiphase Volume Of Fluid to Discrete Phase Model (VOF-to-DPM)	
18	
3.3 Numerical pre-processing.....	23
3.4 Static and dynamic mesh convergence study	30
4. Results and discussion	39
4.1 Newtonian study.....	41
4.1.1 Exit orifice diameter, pressure injection and viscosity effects on	
the liquid sheet stability	46
4.1.2 Primary atomization	56
4.2 Non-Newtonian study.....	65
4.2.1 Non-Newtonian primary breakup.....	71
4.3 Particle Size Distribution (PSD) and spray pattern – Newtonian and	
non-Newtonian comparison	77
5. Conclusion	85
Acknowledgments	90
References	92

1. Introduction

The transition from bulk liquid to droplet dispersed phase, in a gaseous atmosphere, represents an outstanding question in several application fields. Most of them are related to the automotive and aerospace industries, where the injection performance determines the quality of the liquid fuel disintegration and combustion (Lee et al., 2020). Other areas of interest, such as medical device for drug delivery, industrial painting, and electrostatic coating processes, are also open to research on the multiphase atomization modelling (Pendar and Pascoa, 2021; Shi and Kleinstreuer, 2007).

With the advent of the SARS-CoV-2 pandemic, it was clear that sprays and aerosols are of the utmost importance in our daily lives. It suffices

to think of the numerous research activities that, nowadays, aim to understand and model the fluid dynamics of virus-laden droplets into open areas and workplaces (De Padova and Mossa, 2021; G. Seminara et al., 2020; Y. Feng et al., 2020). Accurate predictions of the droplet motion and deposition in indoor environment are essential to analyse health risks. In this regard, special attention is given also to new spray technology designed for the surface disinfection (J.L. Cadnum et al., 2020). The significant consideration for this application field emphasizes the current interest in investigating the key aspects that determine the performance of small-scale cleaning sprayers. From this perspective, the characterization of the atomization process turns out to be crucial for a comprehensive product design study.

Atomization plays a key role in a wide variety of consumer goods, where spraying is needed to distribute liquids, even complex liquids, onto surfaces. In the detergent/cleaning product applications, the features of the spraying device (i.e., the atomizer) are selected to perform a wide spray pattern. To achieve this, the atomizer must expand the output liquid film against the contracting surface tension forces. This is the case of the pressure-swirl atomizer, where the pressure energy is converted into kinetic energy that leads a swirling liquid to produce a core of air, resulting in a hollow-cone spray (Amini, 2016). The latter will be object of interest of this work. We are interested in investigating the key aspects of a laminar swirl flow produced by a pressure-swirl atomizer. The geometric configuration of the device and the properties of the gas and liquid phases can affect the attributes of the multiphase spray (Lefebvre and McDonell, 2017).

The entire picture then requires the study of a multiphase flow within the nozzle, the outer displacement of the liquid-gas interface and the droplet spread into the atmosphere. We investigate through Computational Fluid Dynamics (CFD) the stability of the swirling liquid sheet by solving the fluid dynamics both in the bounded in-channel flow and in the unbounded free-surface flow, simultaneously. The stability investigation of the pressure-swirl spray represents a useful and innovative tool to predict the spray performance in terms of hollow-cone failure modes. From an applicative point of view, the detection of undesired spray configuration aid in improving the product technology.

Through a detailed study of the characteristics of the hollow-cone spray device, an optimization process can be performed by identifying the fluid/packaging main parameters that affect the product quality.

In the following sections, we will show the capability of an innovative numerical predictive model with the computational support of the commercial software ANSYS Fluent. Compared to the actual field of research advancements, we exploit this CFD model to predict and recognize specific fluid dynamics phenomena and, most importantly, operability limits of the hollow-cone spray process.

A completely new characterization of the swirling liquid film configuration at short and long distance from the atomizer nozzle will be shown. We describe how the key parameters such as pressure injection, nozzle exit orifice diameter and Newtonian/non-Newtonian rheological behaviours affect spray properties and topology before and after the breakup of the liquid sheet into droplets.

2. State of art

The first attempt to describe how a liquid jet disintegrates dates back to Lord Rayleigh (1878), who proposed a theory for ligaments breakup into drops. The simplest configuration investigated by Rayleigh was a Newtonian liquid column ejected from a circular orifice in a stagnant fluid, where the velocity lies mainly along the axial direction. He observed that the instability condition that determines a droplet detachment from the bulk liquid body is related to the critical wavelength that ensures the fastest growing disturbance on the liquid surface. At stationary feeding flow and low flow rate, the liquid is issued drop-by-drop close to the nozzle due to an absolute instability determined by the surface tension and gravity forces. This condition is

named dripping regime. Conversely, when the velocity increases, the instability is convected away from the nozzle, giving rise to the jetting regime, in which a cylindrical-shaped jet is obtained. As observed by Lord Rayleigh (1878), the higher the velocity, the further the jet disintegrates from the nozzle exit.

Since then, different scenarios have been considered to analyse the details of jet disintegration under specific flow conditions (Zhao et al., 2020; Anufriev et al., 2020; Li and Soteriou, 2016). Regarding the flow inside the nozzle, instead, Rocha et al. (2015) emphasized the benefits and the capabilities of the axially induced swirling pipe flow for phase segregation in laminar flow conditions ($Re < 2000$), using a CFD package for the numerical analysis.

In the atomization process, density, viscosity and surface tension affect the spray performance. Therefore, the Reynolds ($Re = \rho_L \bar{u} D_o / \mu_L$) and Ohnesorge ($Oh = \mu_L / \sqrt{\rho_L \sigma D_o}$) numbers quantify reliably the competition among inertial, viscous and surface tension forces acting at the gas-liquid interface. A jet issuing in ambient gas can experience different dynamics depending on the liquid properties and operating conditions. As shown in Figure 1, through a non-dimensional analysis, it is possible to characterize how a straight jet disintegrates (Shao et al., 2018; Lefebvre and McDonell, 2017; Dumouchel, 2008; Ohnesorge, 1936). In the region 1 of the Figure 1, i.e., at low Re and Oh -values, the Rayleigh mechanism is expected, where the jet breaks up exclusively because of surface tension forces. By crossing to region 2,3,4 one ends up to pure atomization, where the jet disintegrates as soon as the liquid spreads out from the orifice due to aerodynamic interactions. The four

different regimes are distinguished by various jet break-up time/distance and average drop diameter. Spray may be carried out in several ways, and different factors do affect spray performances. The atomizer configuration, gaseous medium and liquid properties influence the jet morphology and the various liquid structures (i.e., blobs, filaments, droplets) displacement into the environment.

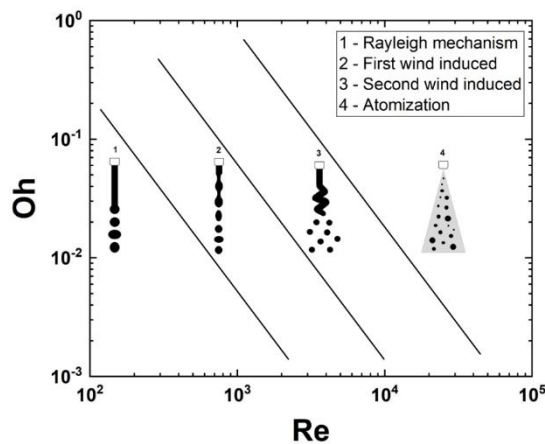


Figure 1 – Classification of modes of disintegration for a straight jet (adapted from " Shao, C., Luo, K., Chai, M., Fan, J., AIP Advances, Vol. 8, ID 045211, 2018; licensed under a Creative Commons Attribution (CC BY) license.").

More complex atomizer configurations have been considered depending on the specific application requirements (Wu et al., 2021; Vegad et al., 2019; Sinha et al., 2015; Sallam et al., 2002). When applications demand wide spray patterns, they are achieved by forming liquid sheets instead of straight jet. In this case, specific devices could be implemented to further expand the ejected liquid sheet against the contracting surface tension forces (Sirignano and

Mehring, 2000). The simplex pressure-swirl atomizers achieve this condition by making the fluid flowing through tangential holes, imparting a resultant swirling motion (Rajamanickam and Basu, 2017; Amini, 2016; Sivakumar and Raghunandan, 2002). In these devices, the liquid emerges from the discharge orifice as an annular sheet, in which both the liquid bulk sheet and the detached droplets spread radially outward to form a hollow-cone spray (Shim et al., 2008).

The viscosity of the liquid has a prominent role in the hollow-cone atomization process. It exerts a stabilizing effect by inhibiting the growth of the disturbances on the liquid-gas interface, delaying the first disintegration (Lefebvre and McDonell, 2017). Yao et al. (2012) observed, experimentally, that more viscous fluids result in smaller average spray cone angles. As the liquid viscosity increases, the cone collapses earlier with larger droplets in the final stage (Yao et al. (2012)). The possible non-Newtonian behaviour of the liquid, most importantly a viscoelastic behaviour, can strongly affect the primary break-up (Keshavarz et al., 2015; Keshavarz et al., 2016; Rezaeimoghaddam et al., 2010). Rezaeimoghaddam et al. (2010) focused their study on modelling non-Newtonian power-law fluid flow within simplex atomizers. They highlighted the influence of the flow index n on the spray cone angle by considering shear thinning and shear thickening fluids.

The surface tension of dispensing liquid plays a key role in the atomization process, since it represents the force that opposes the formation of new surface area. A decrease of this physical property alters the breakup length while it increases the spray angle (Davanlou

et al., 2013). Davanlou et al. (2013) observed that adding surfactants reduces the surface tension coefficient and, consequently, improves the spreading factor of the droplets produced by simplex pressure-swirl atomizers. In different spray applications, where surface active agents are mixed with the bulk liquid, surface tension could not be considered as a constant property of the liquid surface (Shavit and Chigier, 1995). The variation of the surfactant concentration at the liquid-gas interface promotes a dynamic change of the surface tension over the dispensing time. This phenomenon is due to the transient migration of the surfactant molecules that terminates once the surfactant concentration is high enough to establish the equilibrium condition between the bulk and the free-surface of the liquid (Shavit and Chigier, 1995).

The breakup processes of pressure-swirl sprays with helical grooves have been studied by Prakash et al. (2014), focusing mainly on the interactions between the conical swirling liquid sheet and a gaseous cross-flow at long distance from the nozzle exit. Concerning the hollow-cone spray without the air cross-flow, the pressure swirl jet exhibits different breakup stages by increasing the Weber ($We = \rho \bar{u} D / \sigma$) number, i.e., the dimensionless number comparing inertial and surface tension forces. The experiments show that the spray half-cone angle ranges around 15-33° with a swirl number (based on the atomizer configuration) equals to 1.3 (Prakash et al., 2014).

Ding et al. (2016) and Saha et al. (2012) investigated the primary and secondary break-up/atomization mechanisms of a hollow-cone swirling spray. During the primary atomization, the liquid sheet disintegrates and takes the shape of ligaments, blobs and droplets.

Subsequently, large part of the droplets produced in the first step of fragmentation interact with each other and either coalesce, collide, or break down into smaller droplets, giving rise to the secondary atomization (Lefebvre and McDonell, 2017; Ding et al., 2016; Saha et al., 2012).

Upstream from the primary atomization, the internal flow within the nozzle atomizer and the liquid-air interaction at the nozzle exit, i.e. the air-core dynamics, do affect the spray characteristics and its stability (Maly et al., 2018). The inception of the air core is due to the radial pressure gradient promoted by the swirl that is, in turn, greatly influenced by the nozzle geometry dimensions (Som, 2012). Som (2012) thoroughly investigated the correlation between the simplex swirl nozzle design, the air-core formation and the corresponding liquid sheet thickness and velocity. From his study, it clearly appears that, depending on the pressure-swirl nozzle dimensions, two limiting values of the Reynolds number can determine the air-core formation and its fully developed state within the nozzle geometry.

Recently, Laurila et al. (2020) and Laurila et al. (2019) investigated both experimentally and numerically the main pressure-swirl characteristics of a viscous fluid flow into a large-scale swirl nozzle with a single inlet. They analyzed the velocity fields and the flow structures of the swirling liquid along both the internal geometry sections and the external environment until the inception of the primary atomization. The conical liquid sheet exhibits different morphologies at different Reynolds numbers evaluated at the inlet section, while the air-core arises only at $Re > 1500$ with a helical shape.

Their results show the formation of the conical liquid sheet also with a small air-core, which, consequently, does not represent a prerequisite to generate a hollow-cone spray of Newtonian viscous fluids.

It so appears that both micro-scale and macro-scale phenomena are relevant in the pressure-swirl spray process. Consequently, due to the wide variety of time and size scale ranges, the analysis of this kind of complex systems turns out to be costly from either the experimental or the computational point of views (Li and Soteriou, 2013).

For a high-fidelity simulation of the swirling liquid-gas interface within and outside a complex geometry, high-performance computing (HPC) resources and a robust numerical framework are required (Li and Soteriou, 2013). Indeed, in the literature most of the numerical studies focus their attention either on liquid internal flow in a complex nozzle geometry or on outer ligament formation, with one boundary inlet fixed to mimic the injector exit (Shao et al., 2018; Shao et al. 2017; Fuster et al., 2009; Desjardins et al., 2008; Gorokhovski and Herrmann, 2008; Menard et al., 2007; Bianchi et al., 2007; De Villiers et al., 2004). Shao et al. (2017) conducted a detailed investigation on the numerical simulation of the hollow-cone spray process by implementing a mass conservative level set method. They considered both laminar and turbulent inflow conditions for an annular liquid sheet. Depending on those flow-regime conditions, they showed different velocity fields, recirculation zones and spray patterns that may affect the ligaments/droplets distribution and, consequently, the atomization quality. Fuster et al. (2009) and Shao et al. (2018) dealt with sheet, ligament and droplet formation using Volume-Of-Fluid method (VOF)

coupled with adapted mesh refinement (AMR) technique in GERRIS code. Shao et al. (2018) recently reported direct numerical simulations of primary swirling liquid atomization for combustion applications in GERRIS code.

3. Mathematical model and simulation setup

A multiphase model is implemented in ANSYS Fluent to better understand the fluid dynamics of a swirling liquid flowing from within the nozzle into the air. The modeling and the simulation of the spray process are structured in two stages: the investigation of the hollow cone spray morphology at small distance from the nozzle exit and the study of the conical liquid sheet fragmentation with the corresponding spread of droplets into the open environment.

First, we focus the attention only on the liquid-gas interface displacement at small distance from the nozzle exit. In this regard, we solve the multiphase flow by using the VOF method, which, among other approaches such as Eulerian-Lagrangian or exclusively

Lagrangian for dilute sprays, stands out as flexible and efficient to treat complicated free boundary configurations (Tonini et al., 2008; Lippert et al., 2005; Hirt and Nichols, 1981). Zahedi et al. (2014), Yujie et al. (2012) and Jeon et al. (2011) performed numerical simulations by adopting the VOF model in ANSYS Fluent to analyze the bubble formation and its dynamics for several fluid properties and operating conditions. Apart from the VOF method, other two interface-capturing approaches are widely used in literature: the level-set (LS) and the phase-field (PF) methods (Mirjalili et al., 2017). All of them are included to the category of the one-fluid formulation technique to model two-phase flows. Despite of the advantages of the level set method in terms of accurate computation of the curvature and straightforward extensions to Cartesian adaptive mesh refinement (AMR), this model does not completely satisfy the mass conservation of multiphase flows (Mirjalili et al., 2017). The phase-field method, instead, exploits the thermodynamical equilibrium law to reproduce a more realistic shape of the interface and modifies the transport equation of the indicator function by including physical properties that belong to thin interfaces (Mirjalili et al., 2017).

The Volume Of Fluid - to - Discrete Phase Model (VOF-to-DPM) is, then, implemented to simulate the ligaments and the droplets propagation downstream the primary atomization, at larger distance from the nozzle exit. Compared to the VOF model, in fact, the hybrid VOF-to-DPM exploits both the Eulerian liquid-gas interface tracking (VOF model) and the Lagrangian discrete particle tracking (DPM model). With these methods, we examine in detail the whole

atomization process from the liquid internal flow to the ligaments/particles free-surface flow.

Regarding the mesh generation, the grid discretization adopted in the VOF method is static, while the one used in the VOF-to-DPM method is dynamic. These options allow us to save and optimize the computational resources by implementing customized refinement features in the spray regions of interest (i.e., liquid sheet formation, primary breakup and lumps extension zones).

Both the Newtonian and the non-Newtonian case studies have been carried out by assuming constant temperature, so neglecting the heat transfer equation. Consequently, also the impact of the viscous heating on the fluid flow is ruled out.

3.1 Multiphase Volume Of Fluid (VOF) interface capturing method

The VOF method is a powerful approach used to model two (or more) immiscible fluids not interpenetrating among themselves. It is based on a single set of incompressible Navier-Stokes momentum equations and a transport equation for the volume fraction of one (or more) of the phases. Consequently, for each additional phase added to the model, an auxiliary scalar variable is introduced: the volume fraction of the phase in each computational cell. The presence and the effects of the liquid-gas interface is accounted for the so called CSF (Continuum Surface Force) model proposed by Brackbill et al. (1992).

As for the present case, namely a liquid-gas two-phase system, the governing equations can be written for a Newtonian fluid as in Shinjo and Umemura (2010):

$$\begin{aligned}\nabla \cdot \mathbf{u} &= 0 \\ \rho \left(\frac{\partial \mathbf{u}}{\partial t} + \mathbf{u} \cdot \nabla \mathbf{u} \right) &= -\nabla p + \nabla \cdot (2\mu \mathbf{D}) + \sigma k \delta_s \mathbf{n}\end{aligned}\tag{1}$$

where \mathbf{u} is the velocity vector, ρ the effective density, p the static pressure, μ the effective viscosity, σ the surface tension, \mathbf{n} the unit normal to the interface, k the local curvature of the interface, δ_s a Dirac distribution concentrated on the interface and \mathbf{D} the rate-of-strain tensor, i.e., the symmetric part of the velocity gradient tensor.

The effective local density and viscosity in a computational cell are estimated as:

$$\begin{aligned}\rho &= \alpha\rho_L + (1 - \alpha)\rho_g \\ \mu &= \alpha\mu_L + (1 - \alpha)\mu_g\end{aligned}\tag{2}$$

According to these equations, ρ and μ are calculated as a weighted average of the liquid and gaseous phase density and viscosity (i.e. ρ_L , ρ_g , μ_L and μ_g), and α is the indicator function, respectively.

The indicator function, α , a Lagrangian invariant, is assumed to obey a transport equation of the form:

$$\frac{\partial\alpha}{\partial t} + \nabla \cdot (\alpha\mathbf{u}) = 0\tag{3}$$

Eq. (3) does not contain mass transfer terms on the right-hand side as we are neglecting any kind of mass transfer phenomena (e.g. evaporation-condensation, interphase species mass transfer). The VOF indicator function is updated by solving the convection equation (3), so that the interface can be treated as an internal moving surface. In this way, the volume conservation is guaranteed, and the fluid surface can be located step by step using different algorithms of shape reconstruction. This approach allows the VOF method to reproduce more accurately the liquid-gas phase interaction compared to the other capturing approaches including level set and marker and cell methods (Zhao et al., 2002; Harlow and Welch, 1966; Osher and Fedkiw, 2001).

Concerning the non-Newtonian fluids, we extended the capability of the VOF model by coupling the governing equations with two non-linear viscosity equations. We analysed two kinds of generalized Newtonian fluid models: Power-law and Carreau (Eq. (4) and (5)).

$$\eta = k\dot{\gamma}^{n-1} \quad (4)$$

$$\eta = \eta_{\infty} + (\eta_0 - \eta_{\infty})(1 + \lambda^2\dot{\gamma}^2)^{\frac{n-1}{2}} \quad (5)$$

where η , which substitutes μ_L in Eq. (2), is the viscosity of the generalized Newtonian liquid, $\dot{\gamma}$ the second invariant of tensor \mathbf{D} , k the consistency index, n the power index, η_0 the zero-shear viscosity, η_{∞} the infinite-shear viscosity and λ the relaxation time.

3.2 Multiphase Volume Of Fluid to Discrete Phase Model (VOF-to-DPM)

To reproduce accurately the primary atomization process and the droplets dispersion into the air, we will pass from the VOF method to the hybrid VOF-to-DPM model. The latter is available in Ansys Fluent and is used for applications that include the analysis of the liquid dispersion in gas such as gas turbines or combustion engines (V. Kuznetsov et al., 2019). By applying this model to the hollow-cone spray process, the liquid sheet lump-droplet transition is solved through multiple simultaneous steps (Figure 2). The conical liquid sheet and primary breakup are predicted using the VOF model on a sufficiently fine mesh, while the wide dilute region of the dispersed droplets is simulated by the DPM. The VOF-to-DPM model transition algorithm automatically finds compact liquid masses (i.e., blobs, ligaments, droplets) that have detached from the liquid core in the VOF solution. It then assesses their eligibility for the VOF-to-DPM model transition. If the liquid lump satisfies specified criteria, such as lump size and asphericity (that is, the deviation from the shape of a perfect sphere), it is removed from the resolved liquid in the VOF simulation and converted to a particle in the Lagrangian formulation (Figure 2a). The VOF lump is considered suitable for the conversion into a rigid particle if it fits into the following parameter thresholds:

1. Volume-equivalent sphere diameter range
 - By choosing the minimum and maximum volume-equivalent sphere diameters, the VOF liquid mass whose volume is inside this range is suitable for the conversion. We chose a minimum diameter equal to zero and a maximum diameter equal to the nozzle exit orifice diameter ($D_o = 0.32 \text{ mm}$).

2. Maximum asphericity by radius standard deviation (Figure 2b-(i))
 - For every facet of the liquid-gas interface, the distance between the facet center and the lump center of gravity is calculated ($r_1, r_2, \dots r_i$). The individual distance values are weighted by the size of the individual lump boundary facet. Their standard deviation is computed and then normalized by the average radius. This quantity is zero for perfect spheres, increasingly greater than zero the more the shape deviates from a sphere. All droplets for which this asphericity value is below the specified maximum (equal to 0.5) may be automatically eligible for the transition.

3. Maximum asphericity by radius-surface orthogonality (Figure 2b-(ii))

- For every facet of the liquid sheet surface, a vector from the lump's center of gravity to the center of the lump boundary facet is computed (x_i). This vector is normalized and then used in a dot product with the facet unit normal (n_i) to measure the relative orthogonality. For a perfect sphere, the two vectors are overlapping, hence the value would be 1. All droplets for which this asphericity value is above the specified maximum (equal to 0.5) may be automatically eligible for the transition.

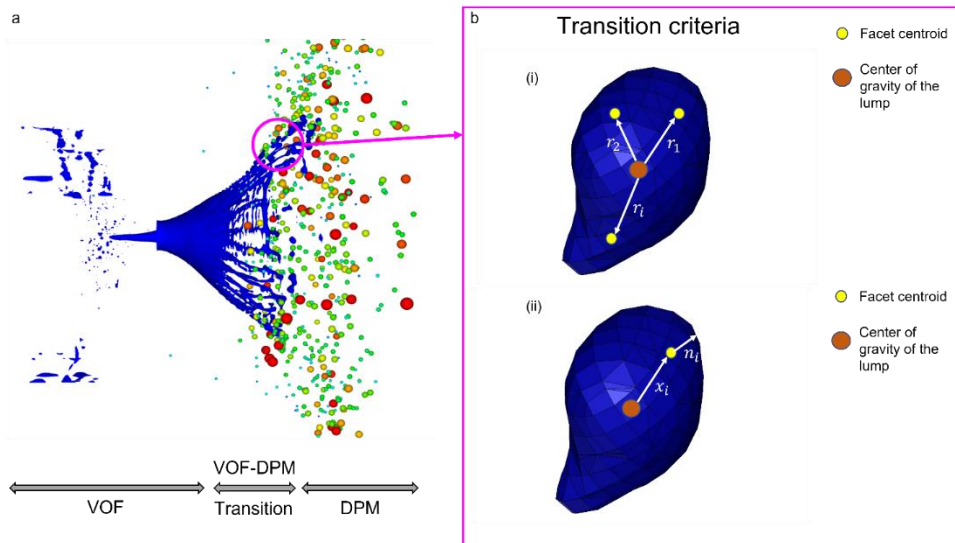


Figure 2 –(a) VOF-to-DPM model description for a hollow-cone spray during the lump-particle transition ($\alpha = 0.5$); (b) transition criteria to establish the conversion from a VOF structure to a DPM particle.

Hence, lumps must satisfy each size and shape-based criteria to get elected for the conversion.

Converting liquid lumps to discrete particles does not impose volume displacement on the continuous liquid phase flow. To avoid spurious momentum sources and mass imbalance, a volume of air with the same volume of the converted liquid lump is created in the VOF simulation to maintain the volume conservation.

Once the particle is generated, the prediction of its trajectory is obtained by integrating the force balance on the particle with the Lagrangian approach. The governing equation that regulates the balance of the particle inertia with the forces acting on the particle, can be written as:

$$m_p \frac{d\mathbf{u}_p}{dt} = m_p \frac{\mathbf{u} - \mathbf{u}_p}{\tau_r} + m_p \frac{\mathbf{g}(\rho_p - \rho)}{\rho_p} \quad (6)$$

where m_p is the particle mass, \mathbf{u}_p the particle velocity, ρ_p the particle density, $m_p \frac{\mathbf{u} - \mathbf{u}_p}{\tau_r}$ the drag force and τ_r the particle relaxation time (Gosman and Ioannides, 1983). The latter is calculated by:

$$\tau_r = \frac{4\rho_p d_p^2}{3\mu C_d Re_p} \quad (7)$$

where d_p is the particle diameter, C_d the drag coefficient and Re_p is the particle Reynolds number. C_d and Re_p are defined as:

$$C_d = b_1 + \frac{b_2}{Re_p} + \frac{b_3}{Re_p^2} \quad (8)$$

$$Re_p = \frac{\rho d_p |u - u_p|}{\mu} \quad (9)$$

where b_1, b_2, b_3 are constants that apply over several ranges of Re_p given by Morsi and Alexander (1972).

Eq. (6) may include additional forces such as the virtual mass force, arisen to move faster the fluid surrounding the particle, or the pressure gradient force due to the fluid motion. However, we consider negligible those forces as they are strongly dependent on the fluid/particle density ratio. We neglect, furthermore, the influence of the particle rotation.

3.3 Numerical pre-processing

The domain adopted for the VOF simulations is made up of a nozzle geometry to which is annexed a cylinder-shaped outer environment (Figure 3a). The detailed size of the geometric design will not be disclosed due to industrial confidentiality reasons.

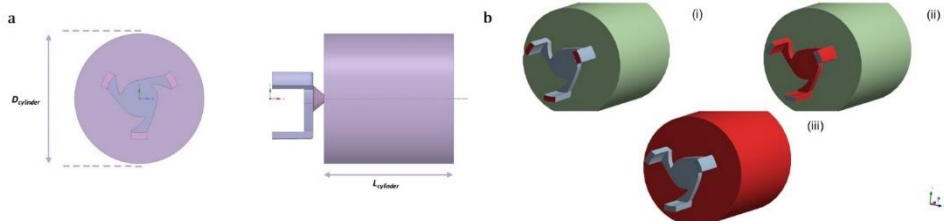


Figure 3 – Domain description. (a) Geometry configuration constituted by a nozzle and a cylindrical domain representing the external environment ($L_{cylinder} = D_{cylinder} \sim 15 D_{orifice} = 5 \text{ mm}$), (b) Boundary conditions: (i) Pressure inlet at the three entrance sections, (ii) No – slip at the nozzle walls, (iii) Pressure – outlet at the external cylinder surfaces.

The three regions in red (Figure 3b) correspond to surfaces where the boundary conditions are imposed:

- (i) A total (gauge) pressure is set at the three branches:

$$P_{inlet} = p_{gauge,total} = p + \frac{1}{2} \rho |\mathbf{u}|^2 \quad (10)$$

while the liquid flow direction is defined normal to the boundary. In Ansys Fluent, to avoid numerical roundoff error, the gauge pressure (p_{gauge}) is used by default to set the

pressure-based boundary conditions. The gauge pressure is obtained by subtracting the operating pressure ($p_{\text{op}} = p_{\text{atm}} \sim 10^5 \text{ Pa}$) from the absolute pressure (p_{abs}):

$$p_{\text{gauge}} = p_{\text{abs}} - p_{\text{op}} \quad (11)$$

(ii) No-slip condition at the walls:

$$\begin{cases} U_x = 0 \\ U_y = 0 \\ U_z = 0 \end{cases} \quad (12)$$

(iii) Pressure-outlet condition at the cylinder surfaces:

$$\mathbf{T} \cdot \mathbf{n} = -p_{\text{gauge,out}} \mathbf{n} \quad (13)$$

where \mathbf{T} is the stress tensor (for an incompressible flow, $\mathbf{T} = -p\mathbf{I} + 2\eta\mathbf{D}$) and \mathbf{n} the unit normal to the boundary surface. The static (gauge) pressure at the outlet is set equal to zero, while the backflow direction is specified normal to the boundary.

It is worth remarking that the boundary condition imposed at the cylinder base at the nozzle exit does not introduce artefacts, indeed we also considered larger cylinders including the nozzle, but the results do not change.

As already mentioned in the Introduction, we characterize the flow within the nozzle and in the external environment. From this perspective, this study determines a time-dependent solution to track and capture the liquid-gas interface as the atomization process proceeds. The initial conditions consider a steady system where the domain is filled by still air ($\alpha = 0$), while the liquid is fed through the three inlet sections.

Laminar flow regime is assumed, as supported by an estimate of the Reynolds number for Newtonian and non-Newtonian power-law fluids (K. Madlener et al., 2009):

$$\text{Re} = \frac{\rho_L \bar{u} D_o}{\mu_L} \quad (14)$$

$$\text{Re} = \frac{\rho_L \bar{u}^{2-n} D_o^n}{k \left(\frac{3n+1}{4n} \right)^n 8^{n-1}} \quad (15)$$

where \bar{u} is the liquid average velocity at the nozzle exit orifice and D_o , as characteristic size, the nozzle orifice diameter. For the characteristics of the liquid properties and for the operating conditions adopted, it turns out that Re is < 2000 , so laminar conditions are attained inside the domain.

Time integration is treated with a first order implicit scheme. Then, the volume fraction of the secondary phase is computed iteratively by solving the scalar transport equation, time step by time step, since it

depends on the other quantities at the current time step evaluated. Its discretized equation has the following form:

$$\frac{\alpha^{n+1} - \alpha^n}{\Delta t} V + \sum_f (U_f^{n+1} \alpha_f^{n+1}) = 0 \quad (16)$$

where $n + 1$ is the index for the current time step, n the index for the previous time step, α^{n+1} the cell value of the liquid volume fraction at time step $n + 1$, α^n the cell value of the volume fraction at time step n , α_f^{n+1} the face value of the liquid volume fraction at time step $n + 1$, U_f^{n+1} volume flux through the face at time step $n + 1$, V the cell volume. As regards the primary phase, there is no additional volume fraction equation.

For the present case, the continuous phase and dispersed phase will consist of air and a Newtonian/non-Newtonian liquid, respectively.

Ansys Fluent handles the spatial reconstruction of the interface using specific schemes. The implicit formulation includes a compressive scheme based on a slope limiter, which prevents from spurious oscillations that may cause abrupt inconsistent changes in the solution domain (Ansys Fluent Guide). This scheme involves a local discretization that defines the value of α in a single cell:

$$\alpha_f = \alpha_d + \beta \nabla \alpha_d \cdot \mathbf{dr} \quad (17)$$

where α_f is the face VOF value, α_d the donor cell VOF value, β slope limiter value, $\nabla \alpha_d$ donor cell VOF gradient value and \mathbf{dr} the cell-to-

face distance. Depending on the value of β that ranges between 0 and 2 (inclusive), a different resolution scheme rate is selected accordingly. To model a distinct sharp interface, the interfacial anti-diffusion option has been enabled. This option reduces the influence of numerical diffusion, which tends to smear the interface sharpness.

ANSYS Fluent CFD solver is based on the finite volume methods. A SIMPLE-type pressure-based segregated algorithm has been selected to solve the governing equations. This algorithm takes advantage by pressure corrections and under-relaxation factors to avoid mass conservation issues. As the spray dispense time is of the order of magnitude of milliseconds, the fixed time step size chosen is 1 μs , while the final integration time is 2 ms. Moreover, special attention will be given to the domain discretization arrangement to provide a mesh that does not affect the solution accuracy.

For the VOF-to-DPM spray study, we started from the geometry and the boundary conditions used in the VOF study, by extending the cylindrical domain shown in Figure 3a (Figure 4). In this way, the primary breakup detection and the subsequent droplet displacement can be performed in a wider environment.

As we are interested in the investigation of the hollow-cone spray pattern on a rigid plane, the boundary condition imposed at the back surface of the cylindrical domain is changed from pressure-outlet to no-slip. As regard the boundary conditions for the discrete phase, instead, we impose that the particles can escape at the front and side surfaces while they are wall-filmed on the back surface of the cylindrical domain. This allows us to examine how the droplets spread

into the environment and their impact against a wall located at 5 cm from the nozzle exit (see L_{cylinder} , Figure 4).

To solve accurately the liquid fragmentation and the atomized droplets, we adopt an explicit VOF method to use a specific spatial discretization scheme for the volume fraction, that is the Geometric Reconstruction Scheme (Geo-Reconstruct Scheme). It is the most accurate approach to represent the interface between fluids through the piecewise-linear method (Ozkan et al., 2007). The first step in this reconstruction scheme is calculating the position of the linear interface relative to the centre of each partially-filled cell, based on information about the volume fraction and its derivatives in the cell. The second step is calculating the advecting amount of fluid through each face using the computed linear interface representation and information about the normal and tangential velocity distribution on the face. The third step is calculating the volume fraction in each cell using the balance of fluxes calculated during the previous step (Ansys Fluent Guide).

With the hybrid VOF-to-DPM method, we also extend the final time up to 5 – 8 ms, based on the time required by the droplet motion to reach the rigid surface located at 5 cm of distance from the nozzle exit. To reduce the computational time, we change the numerical time advancement type from fixed to adaptive. The minimum and maximum time-steps are $1e - 09$ s and $1e - 06$ s, respectively, according to the characteristic time of transit of a fluid element across a control volume, that is the time taken by the fluid to empty out of the cell.

By implementing the adaptive multiphase-specific method, the solution time-step is progressively regulated by the flow and constrained by Courant-Friedrichs-Lewy (CFL) condition. The latter is defined as follow:

$$C = \frac{u \Delta t}{\Delta x} < C_{\max} \quad (18)$$

Where C is the dimensionless Courant number, u the velocity magnitude within the cell, Δt the time-step, Δx the cell size and C_{\max} the constraint to prevent the simulation from numerical inaccuracy or divergence. For the present work, $C_{\max} = 1$.

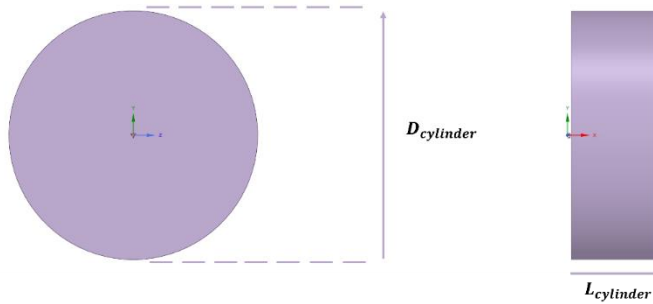


Figure 4 - Geometry configuration constituted by a nozzle and an extended cylindrical domain representing the external environment ($D_{cylinder} = 140 \text{ mm}$, $L_{cylinder} = 50 \text{ mm}$)

3.4 Static and dynamic mesh convergence study

Concerning the mesh, in the VOF study, the domain is divided in three different regions: the internal geometry (1), a region at the nozzle exit (2), and the remaining part of the cylindrical region (3). The resulting static mesh is reported in Figure 5.

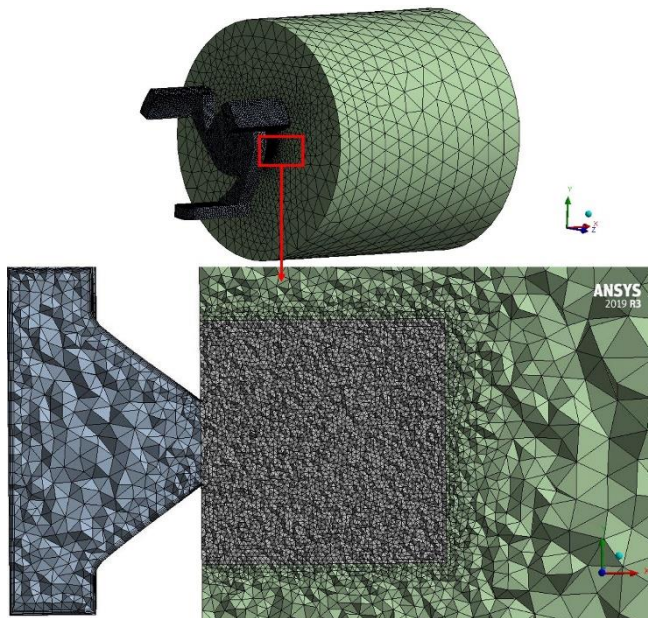


Figure 5 – Overview of the tetrahedral mesh. In the zoom view of a lengthwise plane the connection between the nozzle and the refined region is shown.

It was necessary to verify that the spray calculations were mesh independent. For this reason, the first step of this work carried out a mesh convergence study. The latter was performed in the critical regions where either the velocity magnitude (U) or the volume fraction (α) profiles change significantly, i.e., in region (1) and (2) (see Table I and Figure 6).

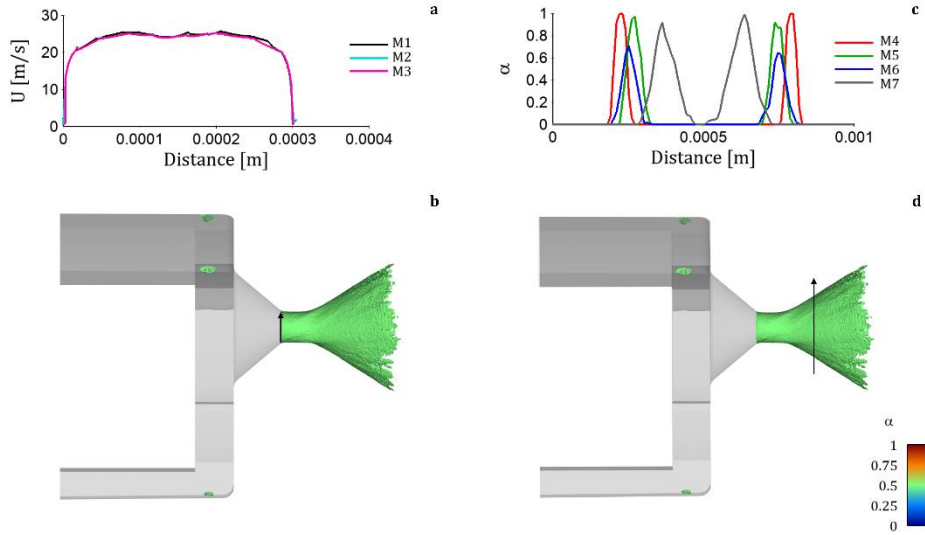


Figure 6 – Grid dependency inspection. (a) Velocity profiles at the exit orifice of the region (1) for different enclosure discretization rates M1, M2 and M3, (b) Volume fraction profiles at the middle of the cylindrical refined region (2) for different discretization rates M4, M5, M6 and M7, (c) Hollow-cone spray ($\alpha = 0.5$) at the computational end time of 2 ms with a black-arrow cut-line at the exit orifice of the region (1), (d) Hollow-cone spray ($\alpha = 0.5$) at the computational end time of 2 ms with a black-arrow cut-line at the middle of the cylindrical refined region (2).

Table I - Regions cell size and corresponding total number of cells.

<i>Mesh – region (1)</i>	Δx (μm)	N_{cells} (thousand)
M1	90	290
M2	100	275
M3	200	250
<i>Mesh – region (2)</i>	Δx (μm)	N_{cells} (million)
M4	10	6,7
M5	20	1,1
M6	30	0.58
M7	40	0.46

Concerning the velocity analysis, we focused on the inner enclosure region (1), while the volume fraction was investigated at the outside

domain where the aerodynamic interactions become significant (2). As the velocity gradients exhibit an abrupt change near the swirl chamber and the nozzle exit orifice, a static refinement was implemented at the enclosure region, keeping unaltered the grid size outside the end-cone tip. We investigated three different grid sizes within the nozzle: M1, M2 and M3 (see Table I). For each one, different velocity curves were evaluated at the nozzle exit and at the final time of 2 ms (Figure 6a).

The different profiles upon refinement progressively overlap. For this reason, we chose to work with the enclosure grid size M2 to guarantee solution quality with reasonable computational effort. The velocity profiles are shown in Figure 6a. Due to the nozzle complex geometry and the aerodynamic interactions, the velocity magnitude increases significantly close to the orifice wall, flattening towards the centre as a plug-flow.

It should be remarked that the velocity in Figure 6a refers to the liquid phase only. Indeed, as shown in Figure 6b, with an isosurface of $\alpha = 0.5$, at the final time, the conical liquid sheet is now spread through the outer domain and completely fills the enclosure. Consequently, at the end time, the liquid-gas interaction mainly involves the conical liquid film in the outer environment. For this reason, the bulk liquid velocity evaluated at the nozzle exit orifice, after the transient period, is not significantly affected by flow fluctuations.

The same grid dependency study has been performed by investigating the indicator function variation. The cylindrical-shaped refining region, located next to the exit orifice, has a size of $D_{\text{ref}} = L_{\text{ref}} = 1 \text{ mm}$. Inside this, different α profiles for four different grid discretization

levels (M4, M5, M6 and M7 in Table I) have been examined (Figure 6c), while the enclosure mesh M2 was kept unchanged. At the middle of the refining zone, the abrupt change of the liquid volume fraction is detected (Figure 6d). In this case also, an isosurface of $\alpha = 0.5$ is shown in Figure 6d. As the liquid film shape is conical, the peaks show the domain area crossed by the dispersed phase, while the central valley indicates the existence of the air-core. Due to the well-known extreme mesh sensitivity of α in the VOF method, the volume fraction profiles do not superimpose. It should be noticed, however, that the scarce overlapping consists of just few microns mismatch among the curves. For what matters the velocity data, the adoption of the mesh M2 determines an average relative error of 2% with respect to mesh M1. Hence, we consider mesh independent solution with body elements size of $100 \mu\text{m}$ (M2) and $20 \mu\text{m}$ (M5) for the nozzle and the outer cylindrical region refinements, respectively. With these sizes, the total number of elements in the domain is about 1,5 million.

The implementation of the VOF-to-DPM model requires, instead, a dynamic mesh adaption, to resolve the finest liquid structures produced by the primary atomization. The mesh topology has been changed from tetrahedral to hexahedral with the adoption of the cut-cell method. The latter minimises the element count, keep the cell aspect ratios low and generate cubic hex-cells suitable for consistent mesh adaption.

To optimize the consumption of the CPU resources required to solve the multi-scale spray system, we customize the grid discretization in accordance with the regions of the domain in which the fluid flow is

solved through either the Eulerian or the Lagrangian approach. We distinguish zones of the mesh at different cell size in line with the characteristic length scales of each stage of the spray process (i.e., liquid flow within the nozzle, liquid-gas interface displacement into the primary breakup zone, breakup length and droplets propagation). For the primary breakup zone, we used again a cylinder-shaped static mesh refinement whose size is $D_{\text{ref}} = 8$ mm and $L_{\text{ref}} = 2$ mm, according to the expected spray penetration of the hollow-cone liquid film (Shao et al., 2018; Lefebvre and McDonell, 2017). Far from the primary atomization region, the liquid-gas interface is not tracked anymore. Consequently, in the rest of the external domain, the Lagrangian approach allows us to increase the static mesh size up to 1 mm.

The dynamic mesh adaption enables an automatic progressive refinement based on cell size-shape criteria and specific field variable variation. For a detailed hollow-cone spray simulation, a liquid volume fraction curvature has been chosen as criterion to progressively refine or coarse the mesh at the liquid-gas interface. The adaption mechanism coarsens all cells with a value below 10^{-14} and refines all cells with a value above 10^{-10} . These values are taken from preliminary VOF simulations, in which we compute the global range of liquid volume fraction curvature.

Since the resolution of the initial mesh is not uniform over the domain, we specify a minimum cell size in the adaption settings, to avoid excessively small cells and, therefore, high Courant-Friedrichs-Lewy (CFL) numbers. The static cell size at the primary breakup zone is 80 μm . By considering the potential minimum liquid sheet thickness

and minimum droplet size for the hollow-cone spray process (Lefebvre and McDonnell, 2017; Saha et al., 2012), we estimate both the minimum cell size and the maximum level of refinement. In this regard, to resolve accurately a conical liquid sheet thickness of around 80 μm and a minimum droplet size of around 10 μm , the cell adaption criteria are chosen by using the following expression:

$$\text{min cell size} = \frac{\text{initial mesh size at the primary breakup zone}}{\text{level of refinement}} = \frac{80}{2^4} = 5 \mu\text{m} \quad (19)$$

In this way, with 4 levels of refinements, the liquid sheet thickness that corresponds to the liquid-gas interface length ($0 < \alpha < 1$) is crossed by approximately 10-15 cells and all the tiny drops by around 2 cells, before the DPM conversion (Figure 7).

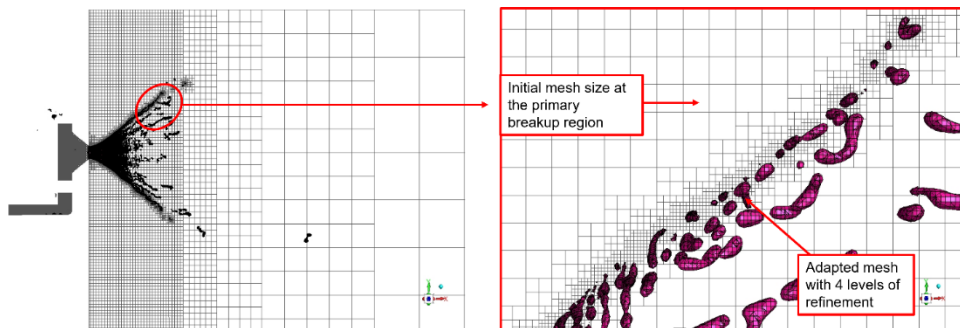


Figure 7 – Cut-cell hex-based mesh with simultaneous static and dynamic grid discretization. The static mesh is gradually coarsened as the flow moves away from the primary breakup zone. The hollow-cone spray (on the left, the lengthwise plane is shown) is finely solved through multiple refinement regions. On the right, there is a zoom-view of the conical liquid sheet breakup solved with the 4-levels adapted mesh.

Table II – Minimum cell size with the corresponding number of hexahedral cells at the primary breakup region.

<i>Mesh at the primary breakup region</i>	Δx_{min} (μm)	N_{cells} (million)
M8	4.5	3.8
M9	5	3.5
M10	5.5	3.1

As regard the dynamic mesh convergence study, a size-based criterion is used to perform it. We change the minimum cell size of the adaptive mesh and compare again the velocity profile at the nozzle exit and the volume fraction displacement into the outer domain (Figure 8).

For the dynamic mesh convergence study, we decrease the viscosity of the fluid to verify the robustness of the numerical code where significant changes of α and U occurs both within and outside the nozzle geometry. We keep fixed the other operating conditions adopted in the static mesh convergence analysis conducted above (Figure 6).

In Figure 8, both the velocity magnitude and the volume fraction profiles with different minimum cell size are shown. In Table II, the corresponding values of the minimum cell size imposed at the primary breakup region are reported. Compared to the static mesh discretization (Figure 6), the implementation of the dynamic mesh adaption improves the accuracy of the solution with a progressive overlapping of the velocity and volume fraction profiles shown in Figure 8a-8b.

The hollow-cone liquid sheet turns out to be finely and accurately solved by using a minimum cell size of 5 μm . A further decrease of the adapted cell size would result in increasing the total number of cells at the primary atomization zone, without improving the grid accuracy of the solution (see Table II and Figure 8).

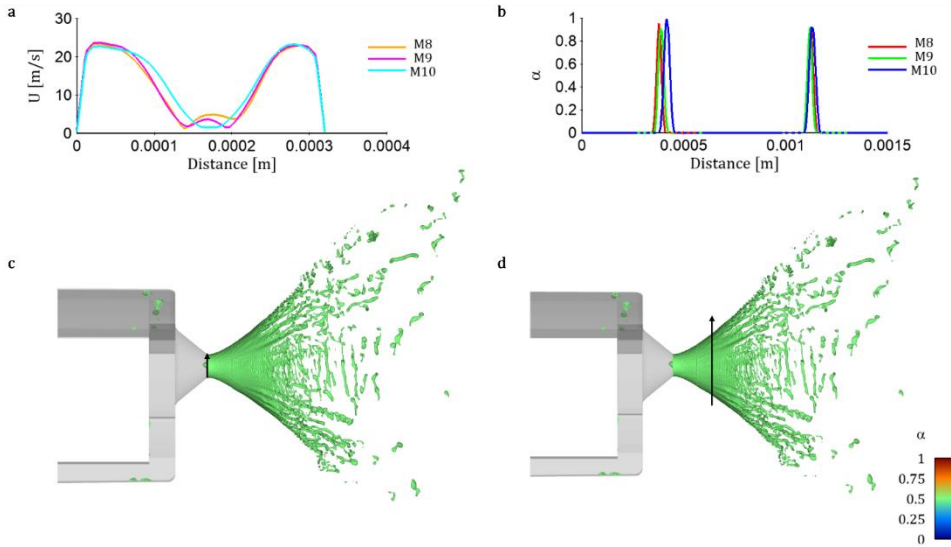


Figure 8 – Grid dependency inspection for the dynamic mesh adaption implemented into the VOF-to-DPM model. (a) Velocity profiles at the exit orifice of the primary breakup region for different minimum cell size of the adapted mesh M8, M9 and M10, (b) Volume fraction profiles within the adapted mesh of the primary breakup region for different minimum cell size M8, M9 and M10, (c) Hollow-cone spray ($\alpha = 0.5$) at the computational end time of 2 ms with a black-arrow cut-line at the exit orifice of the region (1), (d) Hollow-cone spray ($\alpha = 0.5$) at the computational end time of 2 ms with a black-arrow cut-line at 0.5 mm from the exit orifice.

By comparing these profiles with the ones shown in Figure 6, we can appreciate a different fluid dynamic behavior of the multiphase flow. The decrease of viscosity, in fact, strongly affects the characteristic air-core inclusion effect and, consequently, modifies the velocity and the

volume fraction fields of the internal and external domains. Further details about this interesting phenomenon will be provided in the Results and Discussion section.

4. Results and discussion

In this chapter, we present a detailed computational fluid dynamics characterization of the hollow-cone spray process for small-scale pressure-swirl device. With the preliminary VOF study, we perform simulations that qualitatively and quantitatively describe how the liquid sheet morphology and the cone angle are affected by the orifice size, the viscosity and the pressure injection.

For a Newtonian fluid, first we examine the spray development produced by a swirl injection at different liquid viscosities ($\mu_L = 5, 10, 50 \text{ mPa} \cdot \text{s}$), exit orifice diameters ($D_o = 0.25, 0.32, 0.35 \text{ mm}$) and feed pressures ($P_{\text{inlet}} = 4, 5, 10 \text{ bar}$). We started from the analysis of those parameters because they turn out to be of practical interest for

small-scale disinfection/cleaning applications in the field of the hollow-cone spray. Then, we extend that parameter sweep study to investigate more in details the hollow-cone destabilization. The density of the liquid and the gas, instead, are kept constant.

The influence of the surface tension will be analysed through the description of the primary atomization stage by using the VOF-to-DPM model. The role of the fluid cohesive force, in fact, together with the opposed aerodynamic disruptive force, represent a crucial aspect that affect the particle size distribution (PSD). This latter is among the most important parameters that characterize the pressure-swirl spray process. In this regard, the following sections will focus the attention on the fluid/packaging parameters that significantly modify the droplet size and its trajectory.

Moreover, for a non-Newtonian fluid, by implementing both the Power-law and Carreau viscosity equations, we show the relevance of the rheological behaviour in terms of liquid sheet morphology and key operating features.

4.1 Newtonian study

A time-dependent demo study has been carried out to describe the key aspects of the hollow cone spray fluid dynamics. It so appears that once the liquid is injected into the three entrance sections at a given pressure, first it flows within the swirl chamber, where a core of air holds up its rotating motion, then it emerges in shape of an annular sheet from the end-cone tip (Figure 9). The liquid flow first crosses the entrance sections, starts to rotate while it is moving in the swirl chamber towards the exit, then spreads out from the exit orifice generating a hollow-air cone spray.

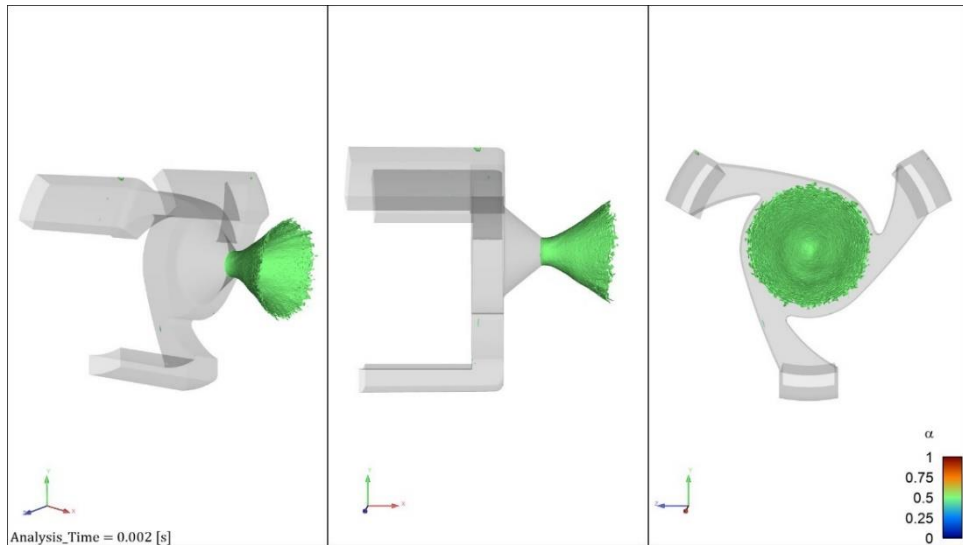


Figure 9 - Multiple views of the hollow-cone formation ($\alpha = 0.5$) at $t = 2$ ms.

The transient air-core penetration, within the nozzle exit and swirl chamber, ensures that the swirling liquid pushes against the walls and, when it is no longer confined by the wall boundaries, it generates a

cone-shaped sheet under the action of the centrifugal forces. After 2 ms the conical shape of the liquid film turns out to be homogeneous and stable, despite of the aerodynamic drag on the liquid-gas interface (Figure 9). All the presented results are taken at 2 ms from the firing. In Figure 10a and 10b the pressure (P) and the velocity contours of a lengthwise cut-plane are shown at the steady state, respectively. The conical shape of the liquid sheet is guaranteed by the transient air penetration within the end-cone tip of the atomizer.

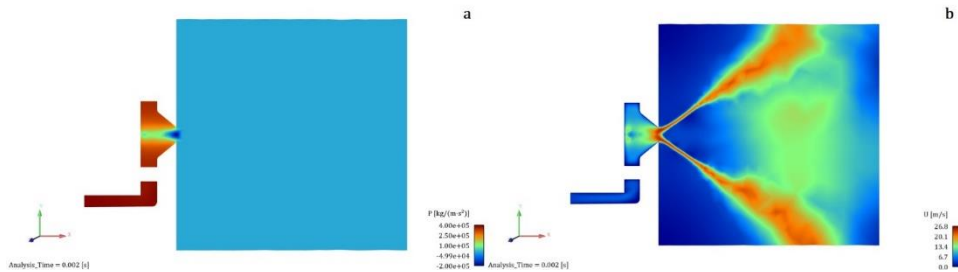


Figure 10 – (a) Pressure contour of a lengthwise cut-plane. (b) Velocity contour of a lengthwise cut-plane.

The swirling motion and the air-core penetration produce a low-pressure zone close to the nozzle exit. In this way, as the liquid flow moves towards the exit orifice, the air penetrates in the opposite direction. This explains why the pressure field shows a significant pressure gradient near the exit orifice (Figure 10a). Likewise, the liquid velocity tends to increase as the liquid flows out from the nozzle. In particular, the velocity field shows a high-velocity annular region, where the hollow-cone spray takes place, and a low-velocity region in the middle of the conical liquid sheet, where the domain is filled by air. At larger distance from the exit orifice the velocity field is less accurate

as calculations are affected by numerical diffusion due to the increase of the cell size (Figure 10b). Our preliminary analysis, however, is focused on the properties of the hollow-cone spray at very small distance from the exit orifice, so the less accurate zone is irrelevant. In the next sections, the model developments will enable to explore the variable fields also at longer distances.

In Figure 11, we also show the streamlines at the same final time of 2 ms. It clearly appears that the symmetric configuration of the three-entrance simplex nozzle provides a significant swirl motion across the internal geometry. As the liquid flows from the swirl chamber to the end-cone tip, a progressive increase of swirl velocity is observed. Then, it reaches the discharge orifice and emerges in form of hollow-cone spray.

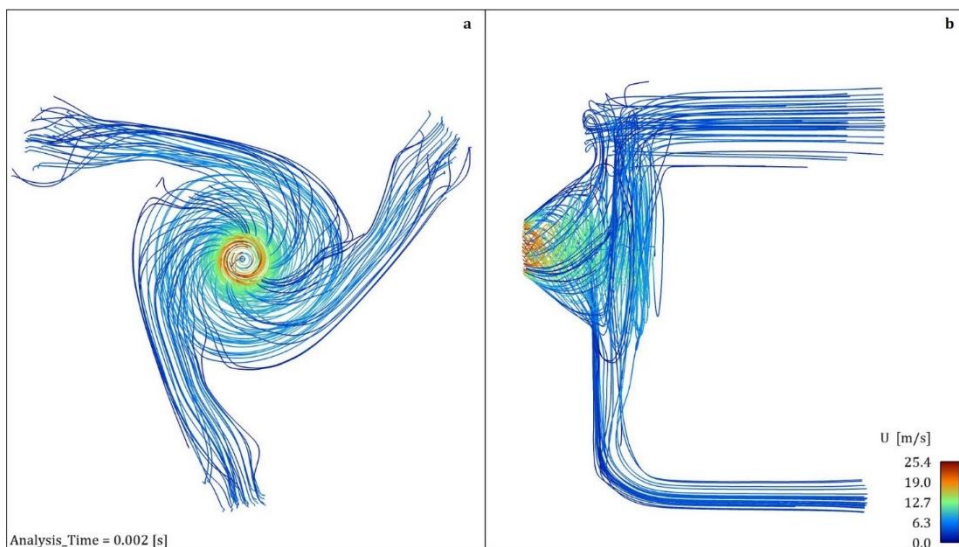


Figure 11 – Streamlines colored by the velocity magnitude within the nozzle geometry at the final time of 2 ms; (a) front view, (b) side view.

To quantify the swirl effect of the liquid flow, we present the results in cylindrical coordinates (r, z, θ) at the exit orifice of the nozzle (Figure 12). For the sake of clarity, θ and r are as follow:

$$\begin{aligned}\theta &= \tan^{-1}\left(\frac{z}{y}\right) \\ r &= \sqrt{y^2 + z^2}\end{aligned}\tag{20}$$

where θ ranges from $-\pi$ to $+\pi$. Then, the axial (U_a), the radial (U_r) and the swirl (U_s) velocity components as a function of θ and Cartesian velocity components U_x , U_y and U_z are:

$$\begin{aligned}U_r &= U_y \cos \theta + U_z \sin \theta \\ U_s &= U_z \cos \theta - U_y \sin \theta \\ U_a &= U_x\end{aligned}\tag{21}$$

As it clearly appears in Figure 12, the dominant velocity components at the exit orifice are the axial and the tangential/swirl ones, while the radial component appears quite negligible. By observing the characteristic symmetric shape of the velocity profiles at the exit orifice, it is evident that the maximum axial velocity is at the centre, while the maximum swirl velocity (in absolute value) is located at the two mid-points between the nozzle exit wall and the centre. It is interesting to notice that, as U_a increases, U_s approaches to zero at the middle region of the exit orifice. This is the reason why the combined action of the liquid ejection, the air penetration in axial direction and the swirl

action, generates a distinct conical thin film, in which the velocity magnitude increases homogeneously from the centre to the edge of the conical liquid sheet (Figure 12).

Moreover, to estimate quantitatively the swirl effect, the swirl number at the nozzle outlet surface (A_o) is evaluated. We calculated the swirl coefficient as the ratio of the axial flux of the angular momentum to the axial flux of the axial momentum (Morris et al., 2016):

$$S = \frac{\int \rho_L U_a U_s r \, dA_o}{R \int \rho_L U_a^2 \, dA_o} = \frac{\int_0^R \rho_L U_a U_s r \, (2\pi r dr)}{R \int_0^R \rho_L U_a^2 \, (2\pi r dr)} \quad (22)$$

where R is the nozzle exit orifice radius.

The swirl turns out to be weak as the swirl number is always $S < 0.6$ in all our simulations. This means that recirculation zones or fluctuations phenomena are not expected (Lilley, 1973). This aspect, and the corresponding typical range of the Re number in our simulations (<1500) supports the assumption of laminar flow conditions. Spot calculations accounting for turbulence through a Large Eddy Simulation (LES) approach, typically adopted for spray simulations, do support laminar assumptions.

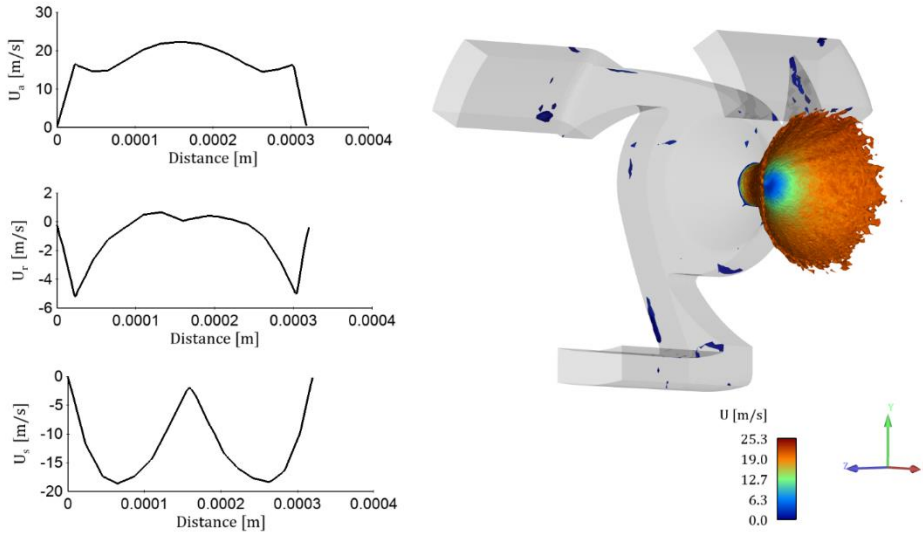


Figure 12 – On the left, axial, radial and swirl velocity components profiles along the centerline of the nozzle exit are shown; on the right, velocity field of an isosurface is presented ($\alpha=0.5$).

4.1.1 Exit orifice diameter, pressure injection and viscosity effects on the liquid sheet stability

As mentioned before, the hollow-cone spray is strongly affected by a wide variety of atomizer features and fluid properties. As regard the nozzle configuration dependence, we focused our attention on the exit orifice diameter. Then, we investigated the effects of the liquid viscosity and the influence of the pressure imposed upstream of the nozzle. Depending on this sweep of parameters, we carried out a global overview of the spray features in terms of cone angle and liquid sheet morphology (Figure 13), for the operating conditions in the Newtonian case reported in Table III.

In Figures 13a-a^l, 13b-b^l and 13c-c^l the exit orifice diameter of the nozzle D_0 is 0.25, 0.32 and 0.35 mm, respectively. It is clear from the volume

fraction fields and the liquid isosurface ($\alpha = 0.5$) that the cone angle changes consistently as the exit hole increases. It so appears that at the smallest diameter the hollow-cone collapses on itself, producing a tube-shaped liquid jet, and the liquid jet is not entirely straight for the swirl motion that imparts a distinctive crumpled shape to the collapsed liquid sheet (Figure 13a^l). Conversely, for larger diameters the hollow-cone forms and has an angle around 75° .

The second set of results, presented in Figures 13d-d^l, 13e-e^l and 13f-f^l, describes how the spray performance turns out to be extremely dependent on the liquid viscosity. As the viscosity increases from $10 \text{ mPa} \cdot \text{s}$ to $50 \text{ mPa} \cdot \text{s}$, the cone angle passes from around 70° to 0° , generating again a long tubular liquid stream. However, in this latter case the jet is completely straight. This means that, at high viscosity and at small distance from the exit orifice, the viscous forces can inhibit and suppress not only the hollow-cone spray pattern, but also any disturbance on the liquid-gas interface (Figure 13f-f^l). We also note that at $\mu_L = 50 \text{ mPa} \cdot \text{s}$, up to 2 ms from the firing with the completely empty nozzle, a considerable quantity of gas remains trapped within the nozzle (Figure 13f^l).

At lower viscosity, instead, air penetration sustains the conical shape of the liquid film. However, at $\mu_L = 5 \text{ mPa} \cdot \text{s}$, aerodynamic interactions are stronger, and a more pronounced corrugation of the free surface is visible. For this reason, the spray pattern at $10 \text{ mPa} \cdot \text{s}$ in Figure 13e^l looks sharper than the one in Figure 13d^l.

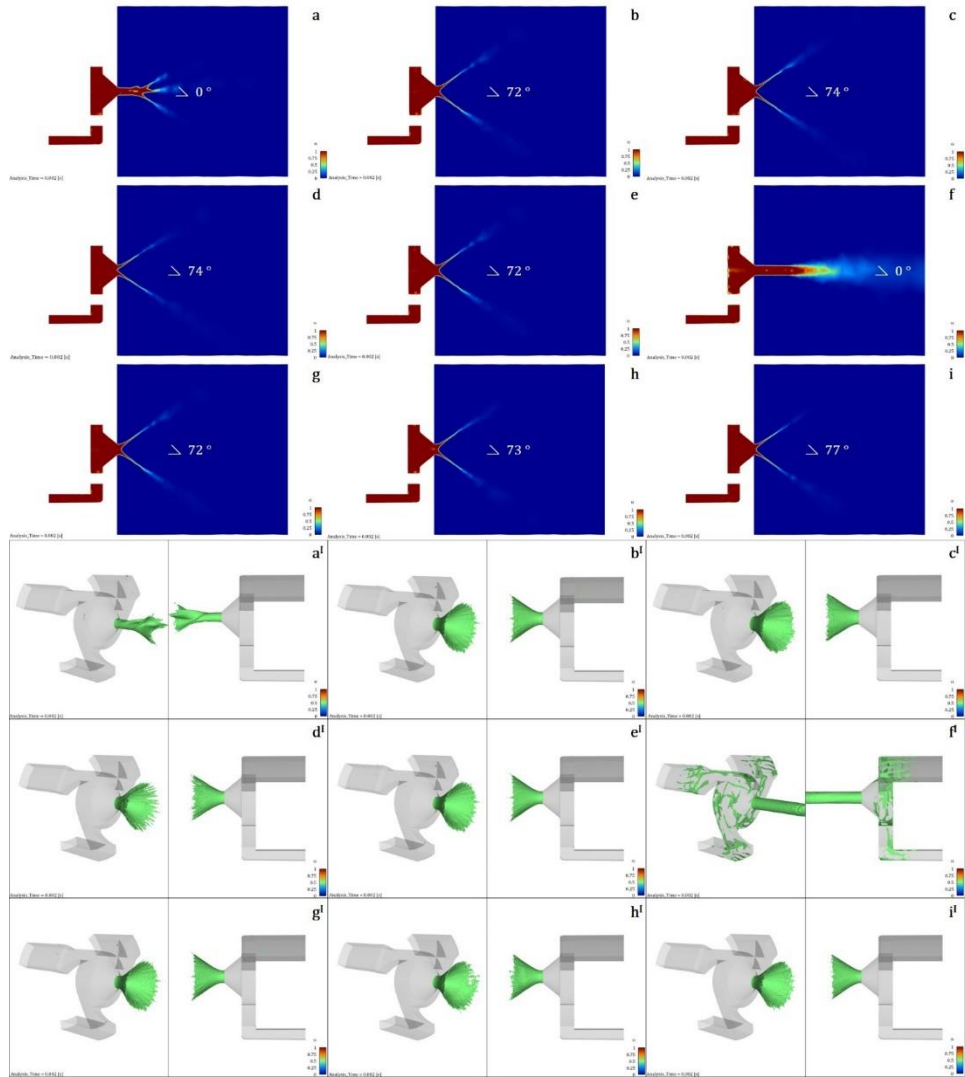


Figure 13 - (a-a') Volume fraction contour of a lengthwise cut-plane and liquid spray pattern using an isosurface of $\alpha=0.5$ (front and side view) at $D_o = 0.25$ mm. (b-b') Volume fraction contour of a lengthwise cut-plane and liquid spray pattern using an isosurface of $\alpha=0.5$ (front and side view) at $D_o = 0.32$ mm. (c-c') Volume fraction contour of a lengthwise cut-plane and liquid spray pattern using an isosurface of $\alpha=0.5$ (front and side view) at $D_o = 0.35$ mm. (d-d') Volume fraction contour of a lengthwise cut-plane and liquid spray pattern using an isosurface of $\alpha=0.5$ (front and side view) at $\mu_L = 5$ mPa \cdot s. (e-e') Volume fraction contour of a lengthwise cut-plane and liquid spray pattern using an isosurface of $\alpha=0.5$ (front and side view) at $\mu_L = 10$ mPa \cdot s. (f-f') Volume fraction contour of a lengthwise cut-plane and liquid spray pattern using an isosurface of $\alpha=0.5$ (front and side view) at $\mu_L = 50$ mPa \cdot s. (g-g') Volume fraction contour of a lengthwise cut-plane and liquid spray pattern using an

isosurface of $\alpha=0.5$ (front and side view) at $P_{inlet} = 4$ bar. (h-h') Volume fraction contour of a lengthwise cut-plane and liquid spray pattern using an isosurface of $\alpha=0.5$ (front and side view) at $P_{inlet} = 5$ bar. (i-i') Volume fraction contour of a lengthwise cut-plane and liquid spray pattern using an isosurface of $\alpha=0.5$ (front and side view) at $P_{inlet} = 10$ bar.

Finally, for $D_o = 0.32$ mm and $\mu_L = 10$ mPa \cdot s, Figures 13g-g', 13h-h' and 13i-i' show the effect of the inlet pressure (from 4 bar to 10 bar). Compared with the preceding cases, the pressure sweep does not determine any qualitative change on the liquid sheet morphology. Quantitatively, though, the cone angle becomes considerably wider as the pressure increases from 5 bar to 10 bar, while between $P_{inlet} = 4$ bar and $P_{inlet} = 5$ bar the characteristics of the spray are nearly identical. For the specific operating conditions and nozzle dimensions adopted above ($Re < 1500$), the stable air-core penetration within the nozzle is not observed. Viscous fluids at moderate velocity, i.e. low Re number, turn out to inhibit the inception of the air-core within the nozzle, without necessarily preventing the conical liquid film displacement (Laurila et al., 2020). In Figure 14 the velocity fields at the nozzle exit orifice of two Newtonian fluids at different viscosities are compared, with the other flow conditions kept unchanged. From Figure 14a it clearly appears that the low viscosity liquid promotes the formation of the air-core with a resultant velocity gradient that extends radially from the centre to the wall of the nozzle exit. Conversely, in Figure 14b, the swirl action for a higher viscous fluid is more homogenous over the orifice area and the discharge orifice is exclusively filled by liquid. The absence of the air-core in Figure 14b, hence, produces an inception of

straight jet at the nozzle exit before the hollow-cone configuration, as shown in Figure 13e-f.

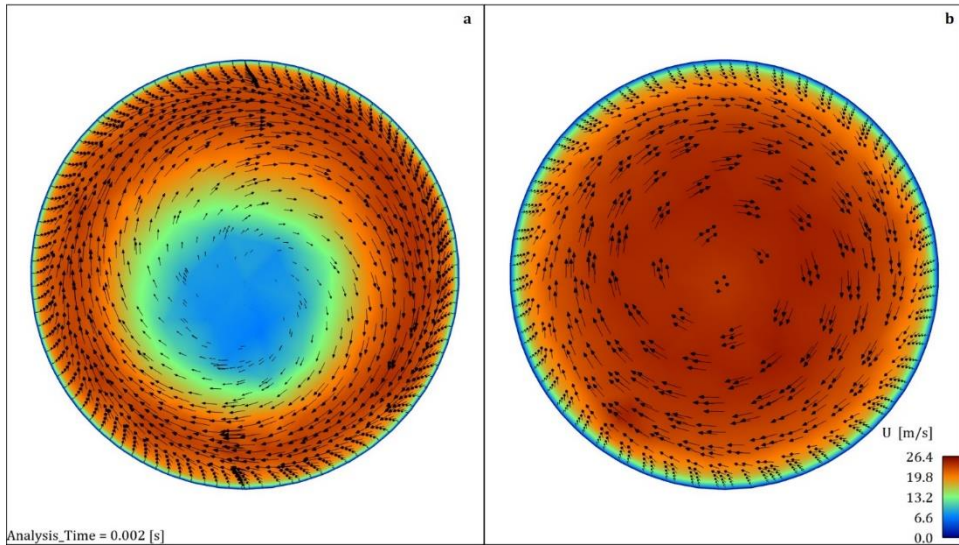


Figure 14 – Velocity (contour and vector arrow) comparison at the exit orifice between (a) $\mu = 2 \text{ mPa} \cdot \text{s}$ and (b) $\mu = 10 \text{ mPa} \cdot \text{s}$ at the same operating conditions and final time of 2 ms.

To characterize the actual geometry of the hollow-cone liquid sheet, we evaluated its thickness, cone angle and jet length as illustrated in Figure 15. The jet length is the extension of the region from the nozzle to the origin of the cone shaped film, and it provides a measure of the tendency to generate a complete straight jet. Regarding the conical film thickness and the cone angle variation, in the literature different experiments have been carried out to find a correlation to predict the geometrical characteristics of the large-scale pressure-swirl spray (Rizk and Lefebvre, 1985, 1987).

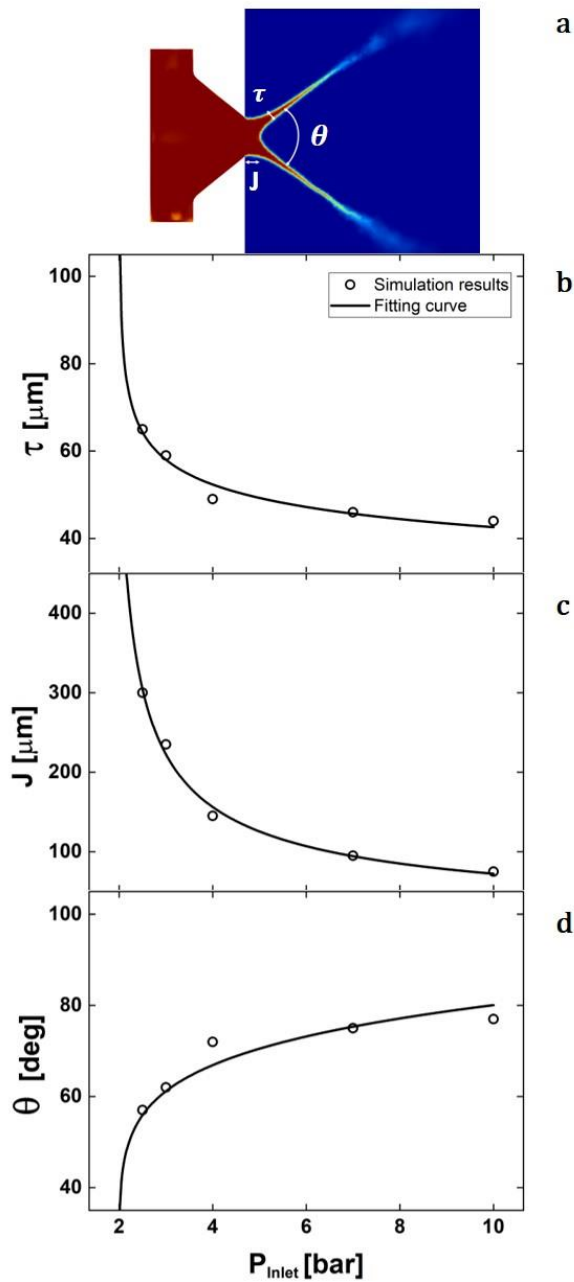


Figure 15 - (a) Graphical description of the hollow-cone liquid sheet thickness, cone angle and jet length in a volume fraction contour. Simulation results and fitting curve comparison of (b) liquid sheet thickness, (c) jet length and (d) cone angle versus operating pressure. The operating pressure investigated in the simulations are: $P_{inlet} = 2$ bar, $P_{inlet} = 2.5$ bar, $P_{inlet} = 3$ bar, $P_{inlet} = 4$ bar, $P_{inlet} = 7$ bar, $P_{inlet} = 10$ bar.

Following these studies, a power-law dependence on the pressure for the three geometrical quantities is expected. Figure 15b-d show our simulation results at 2 ms, together with the corresponding power-law best fit. Indeed, our results are suitably described by the following relations:

$$\theta \propto (P_{\text{inlet}} - 2)^{0.13} \quad (23)$$

$$\tau \propto \left(\frac{1}{P_{\text{inlet}} - 2}\right)^{0.15} \quad (24)$$

$$J \propto \left(\frac{1}{P_{\text{inlet}} - 2}\right)^{0.58} \quad (25)$$

Where θ is the cone angle, τ the liquid sheet thickness and J the jet length.

It is evident that, in agreement with the literature, the increase of pressure leads to reduce the film thickness and make the cone angle wider. In the same way, also the tendency to liquid jetting is affected by the pressure injection. We observe that, as the pressure increases, the distance of the hollow-cone from the nozzle tends to zero, and this corresponds to the air-core penetration effect. Finally, it is worth remarking that a critical pressure ($P_c \sim 2 \text{ bar}$, for the adopted set of the other parameters) appears from the fitting. This aspect determines operability limits for the formation of a hollow-cone spray.

In Figure 16 we show the spray pattern modification as the pressure injection decreases from 4 to 2 bar at the same operating conditions of

the results shown in Figure 15. As stated before, a decrease of the feed pressure leads the spray to significantly change its cone angle and morphology. As shown in Figure 16a-16b, we observed the progressive inception of the collapse of the conical liquid sheet and a corresponding jet length elongation. Once the critical pressure is reached, the hollow-cone spray transforms into a straight jet (Figure 16c).

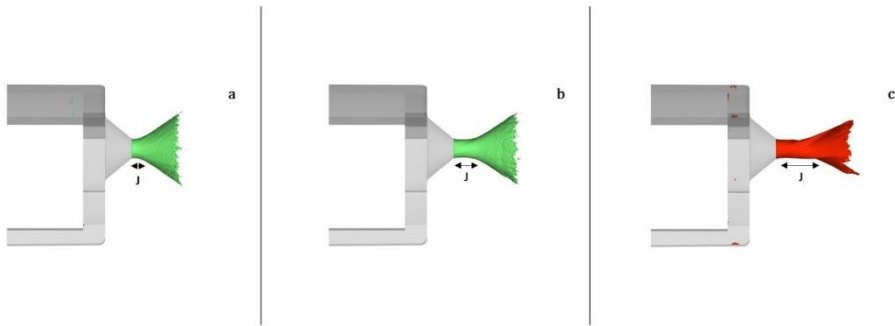


Figure 16 - (a) hollow-cone spray pattern ($\alpha = 0.5$) with $J = 140 \mu\text{m}$ at $P_{inlet} = 4 \text{ bar}$ ($Re = 706, Oh = 0.066$), (b) hollow-cone spray pattern ($\alpha = 0.5$) with $J = 300 \mu\text{m}$ at $P_{inlet} = 2.5 \text{ bar}$ ($Re = 610, Oh = 0.066$), (c) degenerated hollow-cone spray pattern ($\alpha = 0.5$) with $J = 625 \mu\text{m}$ at $P_{inlet} = 2 \text{ bar}$ ($Re = 530, Oh = 0.066$).

Table III illustrates the effects of the relevant dimensionless numbers, namely Reynolds and Ohnesorge. Indeed, different spray morphologies are attained as Re and Oh numbers change (Figure 17). For our hollow-cone spray atomizers, hence, it is possible to distinguish two different atomization regimes: spraying and jetting. In the first case, by increasing Re , inertia forces become significant and lead the swirling liquid to generate a homogeneous and wide spray pattern.

Table III – Operating conditions adopted for the exit orifice diameter, viscosity and pressure injection sweep.

$P_{\text{inlet}} = 4 \text{ bar}$ $\mu_L = 10 \text{ mPa} \cdot \text{s}$ $\sigma = 0.072 \text{ N/m}$ $\rho_L = 1000 \text{ kg/m}^3$			
D_o [mm]	\bar{u} [m/s]	$\text{Re} = \rho_L \bar{u} D_o / \mu_L$	$\text{Oh} = \mu_L / \sqrt{\rho_L \sigma D_o}$
0.25	23.3	582	0.075
0.32	22.1	706	0.066
0.35	18.2	640	0.063
$P_{\text{inlet}} = 4 \text{ bar}$ $D_o = 0.32 \text{ mm}$ $\sigma = 0.072 \text{ N/m}$ $\rho_L = 1000 \text{ kg/m}^3$			
μ_L [mPa · s]	\bar{u} [m/s]	$\text{Re} = \rho_L \bar{u} D_o / \mu_L$	$\text{Oh} = \mu_L / \sqrt{\rho_L \sigma D_o}$
5	23.1	1478	0.033
10	22.1	706	0.066
50	18	115	0.33
$\mu_L = 10 \text{ mPa} \cdot \text{s}$ $D_o = 0.32 \text{ mm}$ $\sigma = 0.072 \text{ N/m}$ $\rho_L = 1000 \text{ kg/m}^3$			
P_{inlet} [bar]	\bar{u} [m/s]	$\text{Re} = \rho_L \bar{u} D_o / \mu_L$	$\text{Oh} = \mu_L / \sqrt{\rho_L \sigma D_o}$
4	22.1	706	0.066
5	22.5	720	0.066
10	28.9	925	0.066

Conversely, in the second case, as Re decreases, viscous forces tend to inhibit the formation of the conical spray. This makes the cone angle narrower and, consequently, worsen the atomization quality.

Despite of the similarity between the described classification of spraying and jetting regimes with the known theory of the vortex breakdown (Billant et al., 1998), some aspects differentiate them. In

fact, such a theory defines the formation of different flow structures in confined swirl jet from a rotating pipe for a liquid phase system (Billant et al., 1998; Douglas et al., 2021). Hence, since our work is based on a laminar liquid-gas flow at low swirl number and our different flow configurations depend on the transient phenomenon of the air-core penetration, there is not a direct comparison. However, both the hollow-cone spray morphology and the conical state of the vortex breakdown turn out to be dependent on the Reynolds number and the swirl effects. Future investigations may provide an effective correlation.

It should be noticed, moreover, that this preliminary analysis does not consider the effects of the inner parts of the nozzle geometry, i.e. swirl chamber and tangential ports sizes.

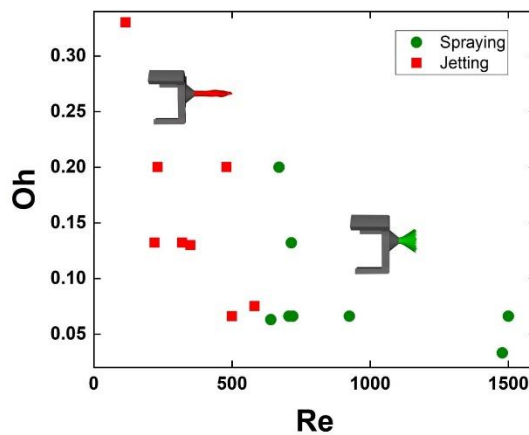


Figure 17 - Classification of two main spray morphology regimes in terms of Re and Oh numbers. The red squares represent simulation results in which we found a rope-shaped jet (jetting). The green circles, vice versa, show numerical results in which the spray exhibits the hollow-cone shape (spraying).

Indeed, a different internal configuration of the device may influence the swirl number at a fixed Reynolds number, with a resultant stabilization/destabilization of the hollow-cone morphology.

In closing this section, we would like to add a remark on the stability investigation of the hollow-cone spray (Figure 17). It is apparent that stable hollow-cone sprays are attained if a critical Re number (around 600) is overcome. In this respect, the effect of the Ohnesorge number, at least in the range of parameters here investigated, seems to be negligible. This stability criterion is of value in designing an effective device depending on the fluid formulation.

4.1.2 Primary atomization

The VOF model allowed us to investigate deeply the liquid sheet displacement within and just outside the nozzle. However, it is restricted by the computational effort that takes to capture accurately the liquid-gas interface and the primary breakup through the Eulerian approach.

As mentioned in the simulation setup section, to track and detect accurately the primary breakup, we improved the mesh refinement and reduced the mesh sensitivity through the implementation of the dynamic mesh adaption in the VOF-to-DPM model.

Starting from the internal flow, we can track and capture time by time the conical liquid sheet displacement, its interaction with the air, the primary breakup and the spray pattern produced by the droplets until

impact against a wall (Figure 18). We get all this data, simultaneously, with a single numerical simulation.

For a stable hollow-cone spray, the periodic detachment of liquid structures occurs along the streamwise direction imparted from the pressure-driven swirl flow. In Figure 18, it clearly appears that, once the liquid is atomized during the first instants of the ejection ($t_{\text{breakup}} \sim t_2 = 0.5 \text{ ms}$), the droplets are spread out radially outwards by directly following the inertial motion of the swirling conical film. In the proximity of the nozzle exit the liquid film turns out to be stretched due to the high relative velocity at the liquid-gas interface. The sheet thickness is, thus, subjected to aerodynamic disturbances on the surface that promote the ligament/droplet pinch-off. As the liquid sheet gets thinner, we observed an increase of the local pressure at the ligament tip contraction that results, first, in a local filament contraction and, then, in a swirling primary breakup.

According to the experimental results conducted by Yao et al. (2012), Prakash et al. (2018) and Ding et al. (2014), the conical liquid sheet breakup turns out to be strongly affected by the liquid viscosity, surface tension and pressure injection. From our numerical results, we found that the increase of viscosity promotes the jetting regime that consequently produces a rope-shaped spray with a little influence of the swirl effect. In this case, the atomization quality is worsened not only in terms of liquid sheet morphology and cone angle, but also in terms of ligament/droplet flow direction, size, and velocity. The impact on the velocity values is significant, especially towards the outer periphery of the spray where the radial velocity component is

weaker than inner locations. At high viscosity, the inhibition of the swirl motion induces a unidirectional motion of the droplets produced by the straight jet along the major axis. This undesired effect is reflected on the resultant reduction of the droplet coverage area on the distant rigid surface.

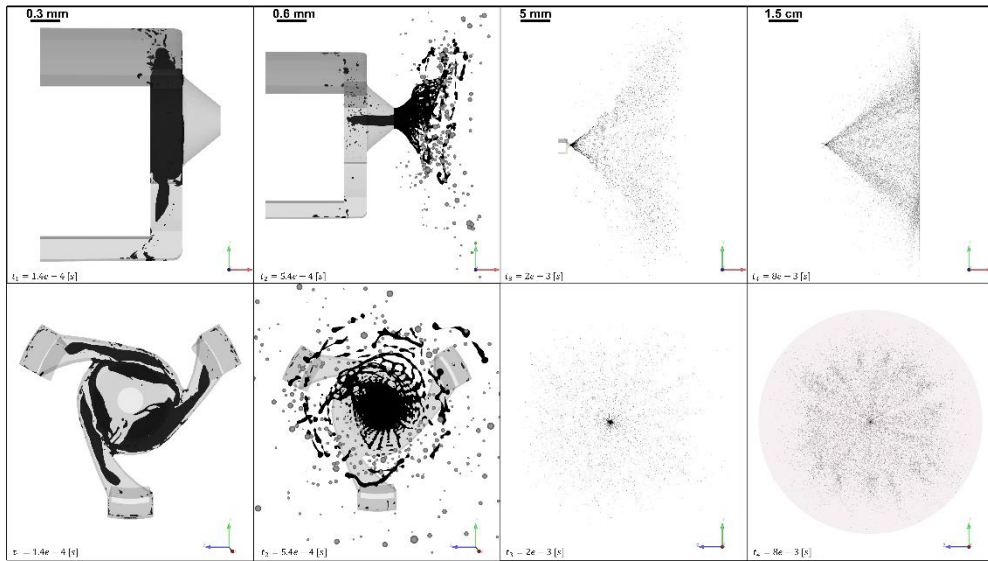


Figure 18 – From left to right, different stages of the time/length multi-scale hollow-cone spray process (the liquid-gas interface is reported at $\alpha = 0.5$). The results are taken at $t_1 = 1.4 \cdot 10^{-4}$ s, $t_2 = 5.4 \cdot 10^{-4}$ s, $t_3 = 2 \cdot 10^{-3}$ s, $t_4 = 8 \cdot 10^{-3}$ s. On the top and on the bottom, we show side and front view, respectively, of the internal and external fluid-particle flow, obtained by performing a single numerical simulation.

An increase of the feed pressure, instead, promote the hollow-cone spray development with a wider spray pattern. The disadvantage of the high-pressure condition is given by the pronounced fluctuated motion of the liquid sheet that does not reach the steady state condition at the final time of 5 milliseconds. The unsteady flapping motion of the hollow-cone spray may randomly disrupt the liquid masses with a

resultant asymmetric ligament and droplet propagation. This phenomenon is due to the high relative velocity that arises at the interface between the liquid and the gas phases (Singh et al., 2020).

Regarding the surface tension effects, both constant and dynamic surface tension properties have been implemented into the numerical code to reproduce the spray process with a typical fluid formulation adopted in industrial applications. The surface tension force depends on the interface curvature. As the curvature radius decreases along the spray penetration direction, surface tension forces become more dominant. As a result, the surface tension strongly affects the annular-shaped primary atomization developed on the thin conical interface.

As reported in the state of art section, the dynamic nature of the surface tension is due to the addition of surfactants in the bulk solution. We model the effect of the surfactant concentration by using a User-Defined Function (UDF), in which we implement the following equation (Shavit and Chigier, 1994):

$$\sigma(t) = \sigma_E + \frac{\sigma_0 - \sigma_E}{\left[1 + \left(\frac{t}{t^*}\right)^n\right]} \quad (25)$$

where $\sigma(t)$ is the dynamic surface tension, σ_E the known equilibrium surface tension (fixed to 0.031 N/m), σ_0 the initial surface tension (assumed to be the surface tension of pure water, equal to 0.072 N/m), t the time, t^* the half-lifetime coefficient, and n the slope coefficient. At fixed surfactant concentration, the half-lifetime coefficient and the

slope coefficient are two constants that were found through a nonlinear curve fitting by Shavit and Chigier, 1994.

By keeping unaltered the operating conditions, we performed two VOF-to-DPM simulations for a Newtonian fluid, in which we analyze the pressure-swirl atomization process of two fluids at different surfactant concentration. The fluid at low surfactant concentration (σ_2) corresponds to $t^* = 7.5 \cdot 10^{-3}$ s and $n = 3.84$, while the fluid at high surfactant concentration (σ_3) results in $t^* = 0.85 \cdot 10^{-3}$ s and $n = 1.91$ (Figure 19). These coefficients have an impact on the time required for the transport of the surfactant molecules to the liquid surface, which is comparable to the characteristic time scales of the breakup mechanisms (order of magnitude of milliseconds).

At the final simulation time of 5 ms, the surface tension of the fluid at low surfactant concentration does not reach its equilibrium value of $\sigma_4 = \sigma_E = 0.031$ N/m, contrarily to the fluid at high surfactant concentration (Figure 19).

During the primary atomization, the dynamic change of this fluid property turns out to affect both ligament morphology and droplet size. In Table IV, we report relevant statistical data derived from transient numerical studies at different dynamic (σ_2, σ_3) and static (σ_1, σ_4) surface tension conditions.

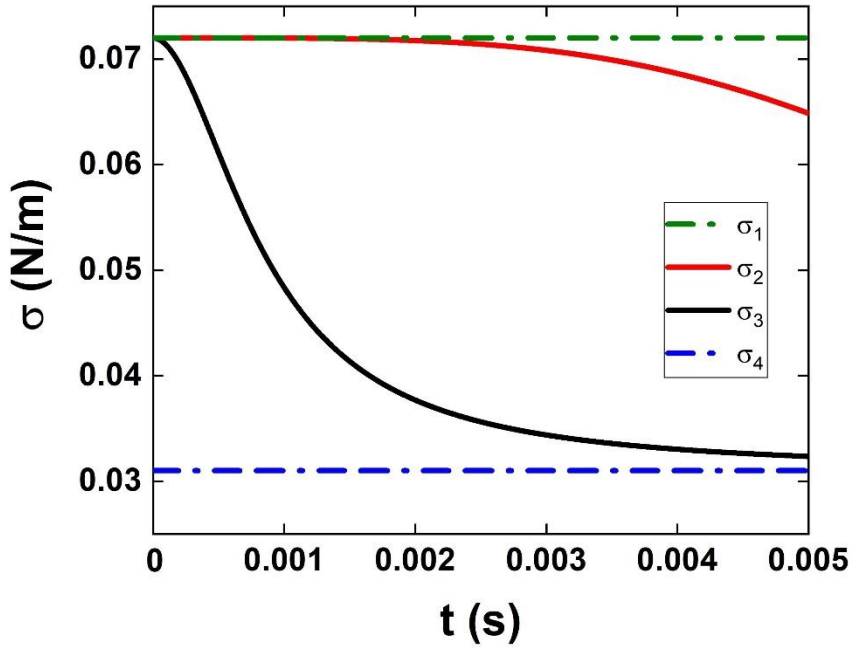


Figure 19 – Static (σ_1, σ_4) and dynamic (σ_2, σ_3) surface tension functions over the dispensing time.

Table IV – Total number of droplets, mean droplet size and standard deviation of the hollow-cone spray at different dynamic and static surface tension values.

$P_{\text{inlet}} = 4 \text{ bar}$ $\mu_L = 10 \text{ mPa} \cdot \text{s}$ $D_o = 0.32 \text{ mm}$ $\rho_L = 1000 \text{ kg/m}^3$			
σ [N/m]	N_{tot}	D_{mean} [μm]	STD. DEV. [μm]
σ_1	9500	49	± 19
σ_2	10200	48	± 18.5
σ_3	12075	45	± 15.5
σ_4	15900	42	± 14.0

The descriptive statistics shown in Table IV is obtained by considering all the discrete droplets generated into the whole external domain from $t = 0$ to $t = 5 \text{ ms}$.

When the surfactant concentration is high (σ_3), there is an increase of the total number of droplets (N_{tot}) produced during the first fragmentation stage, and a decrease of the mean droplet size (D_{mean}) and standard deviation (*STD.DEV.*). The progressive reduction of the cohesive forces promotes the formation of new surface area through a dominant aerodynamic breakup of the liquid structures. When the surface tension is constant and equal to its equilibrium value ($\sigma_4 = \sigma_E = 0.031 \text{ N/m}$), the hollow-cone primary breakup is promoted at a very early stage, with the shortest breakup time/length. Consequently, the minimum mean droplet size and the maximum number of droplets are obtained with a promoted monodisperse spray (Table IV).

Moreover, we notice that the lower the viscosity, the more the effect of the surface tension drop on the spray process is significant in terms of particle size variation.

From a detailed investigation on the influence of the nozzle design parameters on the hollow-cone primary breakup phenomenon, we found out that the swirl number has a strong effect on the hollow-cone spray stability. As in the case for the influence of the fluid properties described above, the nozzle packaging features affect both the spray pattern and the droplet motion. By modifying the three entry ports and the swirl chamber size of the nozzle geometry, we notice that the conical liquid sheet may switch from hollow cone to straight jet configuration, or vice versa, at fixed Reynolds and Ohnesorge numbers. This means that the exit orifice size is not the only geometric parameter that affects the spray performance. As a result, the

configuration and the properties of the hollow-cone spray turn out to be function of Reynolds, Ohnesorge and swirl numbers.

By progressively decreasing the exit orifice area, we observe the transition stage from hollow cone to straight jet mode also in terms of spray pattern and droplets propagation at short and long distances from the nozzle exit (Figure 20). Compared to the distinct annular spray pattern observed when $D_o = 0.32$ mm (Figure 20e-20f), at fixed operating conditions, we notice that the reduction of the exit passage section results in a center-based coverage area of droplets on the wall placed at 5 cm of distance from the nozzle exit (Figure 20). The combined effect of the swirl motion and the progressive collapse induced by the decrease of the exit orifice size, which results in the air-core disappearance, promotes the deformation of the conical liquid sheet and an uneven distribution of particles. This undesired condition may strongly affect the atomization quality of the pressure-swirl spray device.

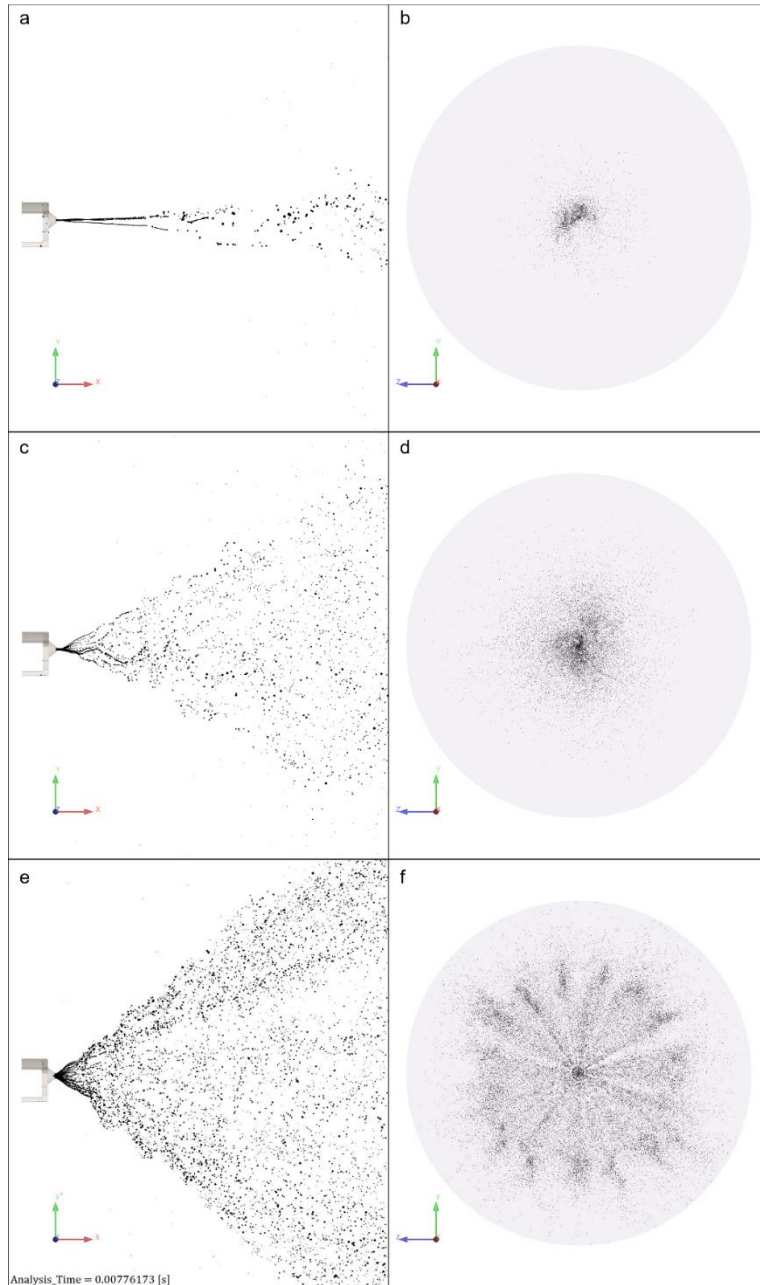


Figure 20 – Transition from the swirling rope-shaped jet to a distinct hollow-cone spray at different nozzle exit size for $t \sim 8$ ms. (a) Side and (b) front view of the straight jet by reducing the total orifice area by 85% with a resultant $D_o = 0.12$ mm. (c) Side and (d) front view of the deformed and uneven conical liquid sheet by reducing the total orifice area by 75% with a resultant $D_o = 0.16$ mm. (e) Side and (f) front view of the hollow-cone spray with no reduction of the exit passage section with a resultant $D_o = 0.32$ mm

4.2 Non-Newtonian study

The liquid viscosity represents the most critical parameter of the hollow-cone spray. In fact, in the Newtonian case study, we have shown how its variation strongly affects the spray performance. Therefore, the possible non-Newtonian characteristics of several fluids of interest in the applications can strongly impact the atomization quality. In what follows, we address the phenomenology of purely viscous non-Newtonian liquids, leaving the contribution of viscoelasticity in future works. In particular, Power-law and Carreau models have been considered. The Power-law constitutive equation implemented in the simulations requires two cut-off values for the viscosity: $\eta_{\min} = 0.001 \text{ Pa} \cdot \text{s}$ and $\eta_{\max} = 10 \text{ Pa} \cdot \text{s}$.

Figure 21 shows the VOF predictions for the two non-Newtonian rheologies at the following operating conditions: $P_{\text{inlet}} = 4 \text{ bar}$, $D_o = 0.32 \text{ mm}$, $\sigma = 0.072 \text{ N/m}$. A completely different liquid sheet morphology is found when a shear thinning ($n < 1$) Power-law or Carreau fluid is considered. We found out that at 2 ms the liquid-gas interface is still unsteady and looks uneven, thin and far less sharp than the Newtonian case. There are several empty areas all around the edge of the liquid film that make the hollow-cone spray not fully developed.

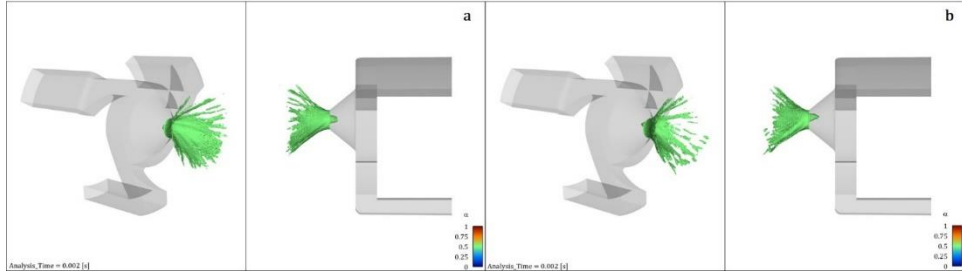


Figure 21 – (a) Spray pattern of a Power-law fluid with $k = 10 \text{ Pa} \cdot \text{s}^{-n}$ and $n = 0.27$. (b) Spray pattern of a Carreau fluid with $\eta_0 = 0.01 \text{ Pa} \cdot \text{s}$, $\eta_\infty = 0.001 \text{ Pa} \cdot \text{s}$, $n = 0.4$, $\lambda = 0.1 \text{ s}^{-1}$.

In addition, if we compare the non-Newtonian with the Newtonian spray pattern, we can observe that, in the first case, the air-core is still present within the end part of the nozzle. This means that, the aerodynamic interactions have a greater impact on the sheet thickness and stability when the liquid viscosity is affected by shear thinning effects.

We already demonstrated that it is possible to distinguish two different atomization modes by properly tuning the viscosity. At specific fluid and geometric properties, when η is equal or larger than $10 \text{ mPa} \cdot \text{s}$, the Newtonian liquid is dispensed in form of jet instead of conical spray. From this perspective, we conducted a VOF study of the non-Newtonian disintegration modes, with the aim of matching the results of the Newtonian case.

In this regard, we made a parametric sweep, firstly, of the consistency index k and, secondly, of the shear-thinning index n , always by keeping unchanged the other parameters.

In Figure 21 there is the comparison between two different power-law fluids, distinguished from two different consistency indexes. The viscosity profiles are coupled with two liquid volume fraction

contours. In this way, it is possible to observe, also for a non-Newtonian fluid, the correlation between the viscosity effects and the liquid sheet shaping. Regardless of the power-law rheological parameter values, η rapidly decreases close to the wall due to the high shear rate, but it tends to increase and reach a nearly constant value in the middle section.

Also in this case, the increment of the liquid viscosity strongly affects the spray pattern.

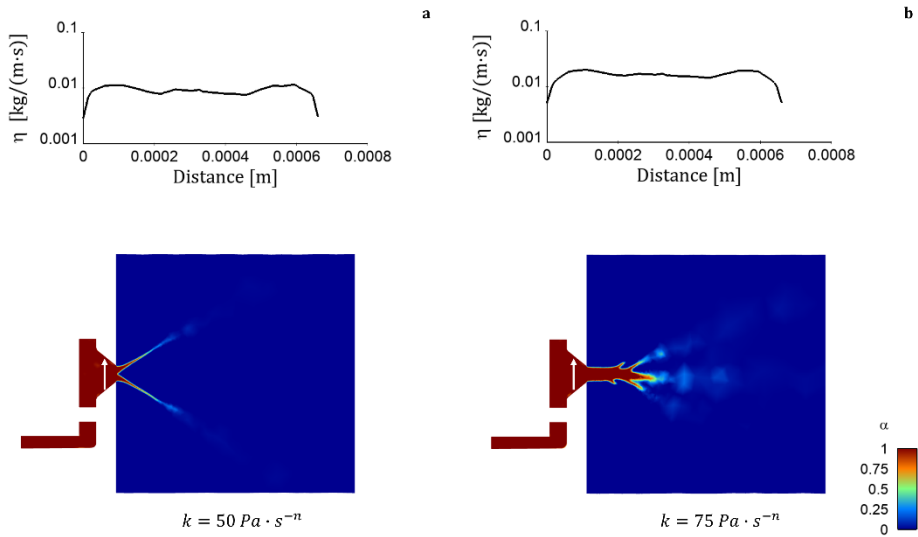


Figure 21 –(a) Semi-log viscosity profile computed with a cut-line (white arrow) at the middle of the nozzle conical end (top) and a volume fraction contour of a lengthwise cut-plane (bottom) of a Power-law fluid with $k = 50 \text{ Pa} \cdot \text{s}^{-n}$ and $n = 0.27$. (b) Semi-log viscosity profile computed with a cut-line (white arrow) at the middle of the nozzle conical end (top) and a volume fraction contour of a lengthwise cut-plane (bottom) of a Power-law fluid with $k = 75 \text{ Pa} \cdot \text{s}^{-n}$ and $n = 0.27$.

In particular, as the consistency index increases, the liquid viscosity, computed at the middle of the conical part of the nozzle (spin

chamber), increases up to exceed that critical value of $10 \text{ mPa} \cdot \text{s}$, giving rise to the transition from spraying to jetting regime.

We now compare the pressure sweep of the power-law fluid shown in Figure 21a ($k = 50 \text{ Pa} \cdot \text{s}^{-n}$ and $n = 0.27$) with the one of the Newtonian fluid at fixed viscosity of $10 \text{ mPa} \cdot \text{s}$ already shown in Figure 15 (section 4.1.1) by analysing aspects of the spray characteristics (Figure 22). Both fluids experience the destabilization of the hollow-cone spray at $P \sim P_c = 2 \text{ bar}$. The reason is related to the similarity between the power-law liquid viscosity, i.e. around $10 \text{ mPa} \cdot \text{s}$ within the nozzle end-cone tip (Figure 21a), with the Newtonian one, i.e. $\mu = 10 \text{ mPa} \cdot \text{s}$.

Moreover, as the pressure increases the cone angles of the Newtonian and non-Newtonian fluids show the same non-linear increase, although the hollow-cone of the power-law fluid seems to be narrower (Figure 22c). As regard the liquid sheet thickness and the jet length (Figure 22a-22b), it appears that at low pressures both τ and J of the power-law fluid show a steeper decrease compared to the Newtonian case. In particular, the jet length of the non-Newtonian fluid even reaches the zero value at high pressures. Those aspects can be explained by considering the sensitivity of the non-Newtonian viscosity to the shear effects that the conical liquid sheet experiences in the external domain. The shear-thinning fluid has a lower viscosity at the hollow-cone interface with respect to the Newtonian one. This lowering promotes the air-core inception and, correspondingly, the reduction of the liquid sheet thickness and the jet length disappearance observed in Figure 22a-22b.

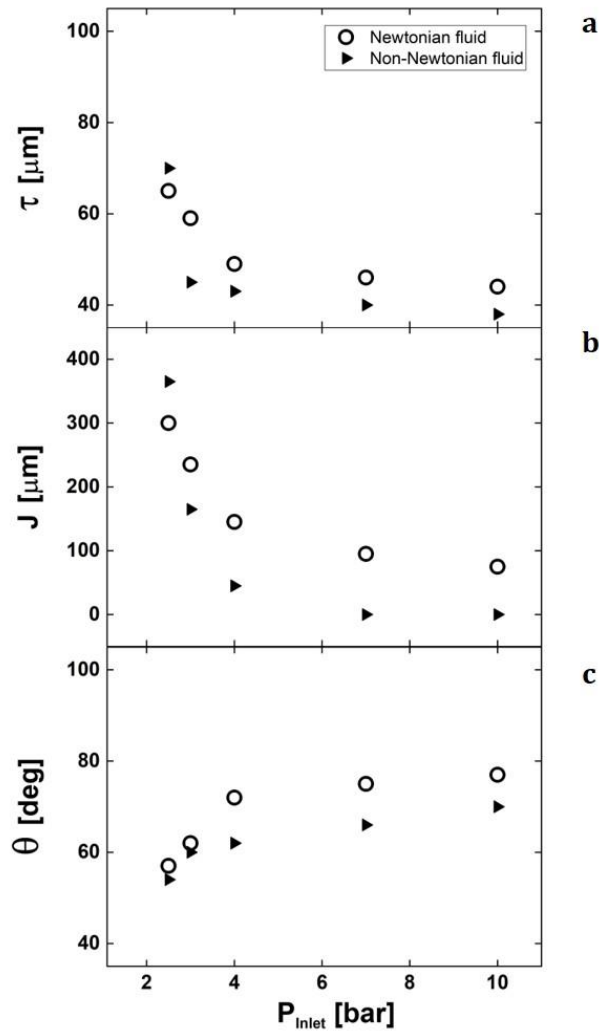


Figure 12 - Newtonian and non-Newtonian fluids comparison of the main properties of the hollow-cone morphology. Simulation results of (a) liquid sheet thickness, (b) jet length and (c) cone angle versus operating pressure for a Newtonian fluid at $\mu = 10\text{mPa} \cdot \text{s}$ and a non-Newtonian fluid at $k = 50\text{ Pa} \cdot \text{s}^{-n}$ and $n = 0.27$. The operating pressure investigated in the simulations are: $P_{\text{inlet}} = 2\text{ bar}$, $P_{\text{inlet}} = 2.5\text{ bar}$, $P_{\text{inlet}} = 3\text{ bar}$, $P_{\text{inlet}} = 4\text{ bar}$, $P_{\text{inlet}} = 7\text{ bar}$, $P_{\text{inlet}} = 10\text{ bar}$.

In Figure 23, we show a global overview of the liquid sheet morphology of different Power-law fluids, in which, under the same

operating conditions, the consistency index k increases from 10 to 100 $\text{Pa} \cdot \text{s}^{-n}$. Two key aspects are summarized in this picture. On one side, at low values of k , the liquid film is conical but it looks really jagged and uneven. On the other side, at higher values of k , the liquid sheet collapses in on itself and the swirl effect tends to increasingly disappear as k increases, creating a long tubular jet. This phenomenon is due to the strict correlation between the increase of k and the increase of liquid viscosity within the nozzle, as showed in Figure 21.

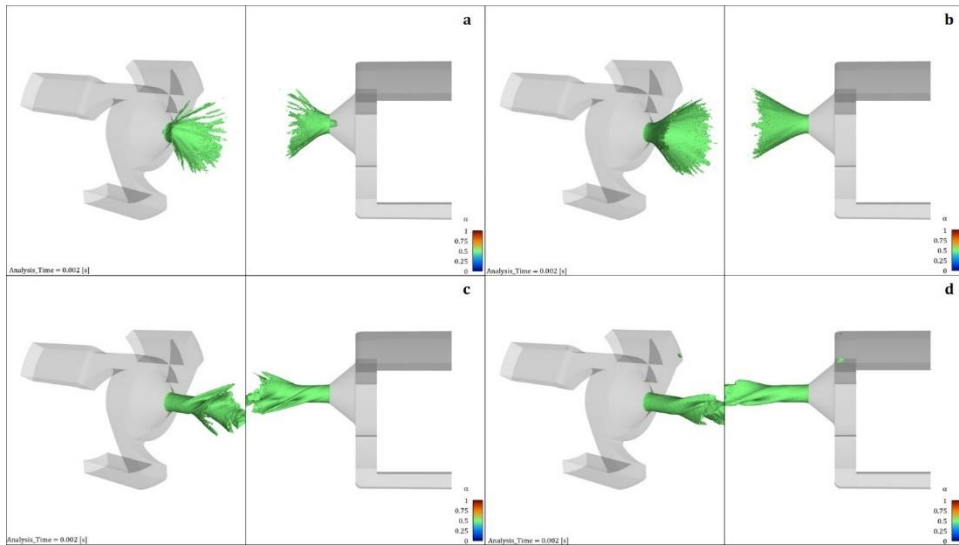


Figure 23 – (a) Spray pattern of a Power-law fluid with $k = 10 \text{ Pa} \cdot \text{s}^{-n}$ and $n = 0.27$. (b) Spray pattern of a Power-law fluid with $k = 50 \text{ Pa} \cdot \text{s}^{-n}$ and $n = 0.27$. (c) Spray pattern of a Power-law fluid with $k = 75 \text{ Pa} \cdot \text{s}^{-n}$ and $n = 0.27$. (d) Spray pattern of a Power-law fluid with $k = 100 \text{ Pa} \cdot \text{s}^{-n}$ and $n = 0.27$.

Moreover, we observed that also the shear thinning index n has a strong influence on the spray performance. To prove such relevance, we analyzed a Power-law liquid with a transition around 10 $\text{mPa} \cdot \text{s}$ within the flow conditions attained in the nozzle.

Indeed, at $k = 50 \text{ Pa} \cdot \text{s}^{-n}$ and $n = 0.25$ the liquid viscosity computed at the middle of the nozzle conical end is still lower than $10 \text{ mPa} \cdot \text{s}$, then the liquid sheet turns out to be hollow-cone shaped.

Conversely, at the same value for k , by increasing n towards a less shear thinning behaviour ($n = 0.32$), the liquid viscosity exceeds that critical value of $10 \text{ mPa} \cdot \text{s}$ and the conical film degenerate into the straight jet. These results support the conclusions derived from the numerical study of the consistency index sweep described above, where different Power-law spray morphologies have been shown. It emerges that both the rheological parameters k and n strongly affect the liquid-gas interface and, consequently, the pressure-swirl atomization quality.

Such evidence gives a hint on liquid formulation to form the spray, when dealing with non-Newtonian fluids. In order to avoid the destabilization of the hollow-cone spray, it is better to deal with Power-law liquids either with viscosity always below the critical one (in this example $10 \text{ mPa} \cdot \text{s}$), or with shear thinning strong enough to make the liquid viscosity lower than the critical one within the nozzle.

4.2.1 Non-Newtonian primary breakup

In this section, we show the results of the primary breakup process of non-Newtonian fluids modelled with Power-law and Carreau viscosity equations.

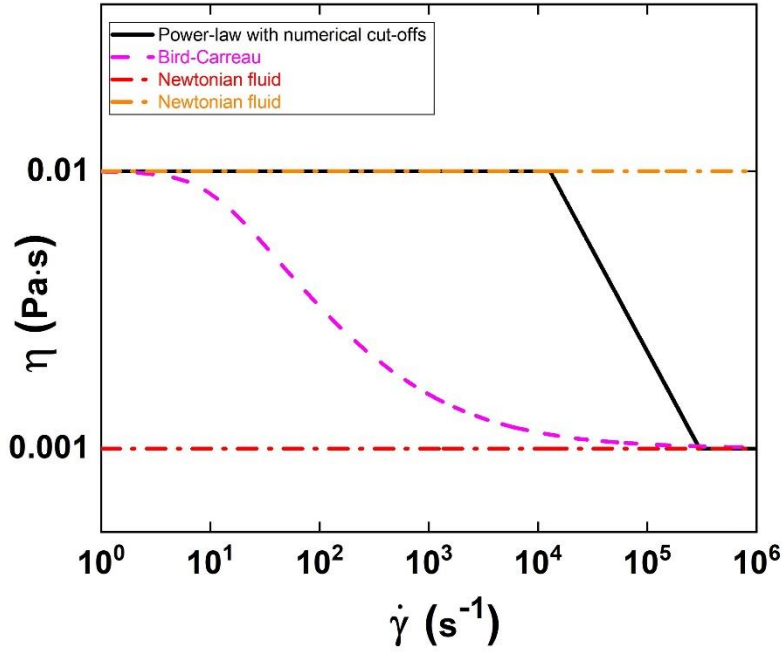


Figure 24 – Newtonian and non-Newtonian liquid viscosity profiles on a logarithmic scale in a wide range of shear rate. The rheological parameters of the Power-law fluid (in black) and Bird-Carreau (in magenta) are, respectively: $k = 10 \text{ Pa} \cdot \text{s}^{-n}$, $n = 0.27$ and $\eta_0 = 10 \text{ mPa} \cdot \text{s}, \eta_\infty = 1 \text{ mPa} \cdot \text{s}$, $\lambda = 0.1 \text{ s}$, $n = 0.4$. The two non-Newtonian fluids, in red and orange, have a constant viscosity of: $\eta = \eta_\infty = 1 \text{ mPa} \cdot \text{s}$ and $\eta = \eta_0 = 10 \text{ mPa} \cdot \text{s}$, respectively.

In Figure 24, the viscosity flow curve for different Newtonian and non-Newtonian fluids is shown. Regarding the power-law model, there are two numerical cut-offs for the minimum and maximum viscosity: $\eta_{\min} = 0.001 \text{ Pa} \cdot \text{s}$ and $\eta_{\max} = 0.01 \text{ Pa} \cdot \text{s}$. We restrict the shear-thinning behavior between those viscosity thresholds to compare the Newtonian and non-Newtonian primary breakup in a specific shear rate and viscosity operating range of application (Figure 24).

As supported by the stability analysis conducted in the preceding sections, the conical liquid sheet does not collapse on itself for the range

of viscosity investigated, but it shows the desired hollow-cone spray configuration for each Newtonian and non-Newtonian fluid (Figure 25).

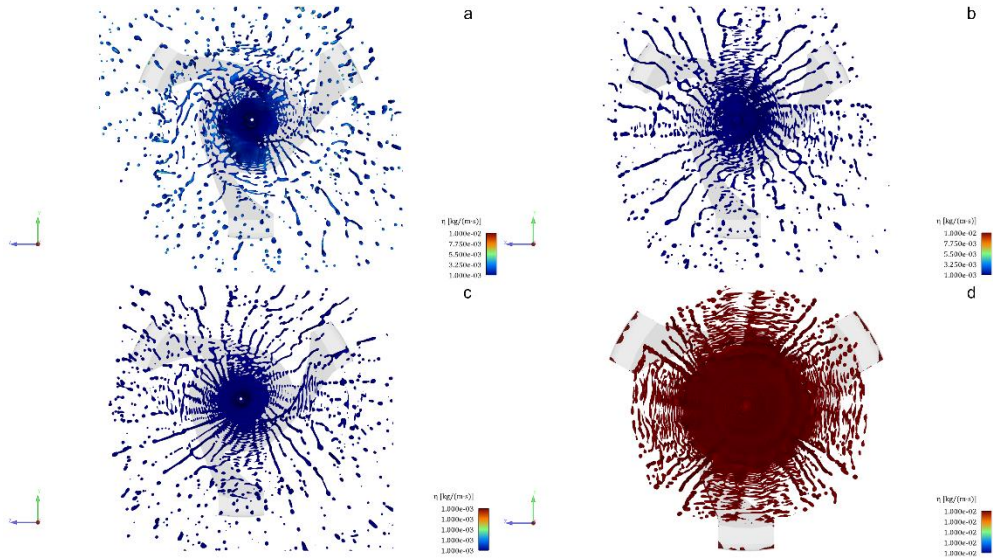


Figure 25 - Zoom of the front view of the Newtonian and non-Newtonian conical liquid sheet fragmentation at 4 mm of distance from the exit orifice and $t \sim 2$ ms. The liquid structures detachment is evaluated for the (a) power-law fluid with: $k = 10 \text{ Pa} \cdot \text{s}^{-n}$, $n = 0.27$, (b) Carreau fluid with $\eta_0 = 10 \text{ mPa} \cdot \text{s}$, $\eta_\infty = 1 \text{ mPa} \cdot \text{s}$, $\lambda = 0.1 \text{ s}$, $n = 0.4$, (c) Newtonian fluid with $\eta = \eta_\infty = 1 \text{ mPa} \cdot \text{s}$ and (d) $\eta = \eta_0 = 10 \text{ mPa} \cdot \text{s}$. The other operating conditions are: $P_{\text{inlet}} = 4 \text{ bar}$, $D_o = 0.32 \text{ mm}$, $\sigma = 0.072 \text{ Nm}^{-1}$.

By looking at the spray pattern of the hollow-cone spray at around 2 ms, we can appreciate different viscosity maps at the liquid-gas interface (Figure 25). Although the liquid film does not destabilize regardless of the fluid properties here adopted, the non-Newtonian behavior affects the primary atomization. According to the rate of deformation of the liquid core at the primary breakup zone, the ligaments produced during the fragmentation of the swirling liquid are perturbed and stressed differently.

This phenomenon is due to the different values of viscosity computed in the range of interest of the shear rate for this application ($10^4 - 10^6 \text{ s}^{-1}$). In this regard, the Carreau fluid behaves like a Newtonian fluid as, anywhere in the spray, the viscosity approaches approximately the plateau value of $\eta = \eta_{\min} = 0.001 \text{ Pa} \cdot \text{s}$. The power-law liquid sheet, ligaments, and droplets, instead, exhibit a viscosity variation, according to the rate of deformation dependence (Figure 25a-25b).

By comparing the non-Newtonian fluids (Figure 25a-25b) with two Newtonian fluids (Figure 25c-25d) that have constant viscosity of $\eta = \eta_{\min} = 0.001 \text{ Pa} \cdot \text{s}$ and $\eta = \eta_{\max} = 0.01 \text{ Pa} \cdot \text{s}$, respectively, we can appreciate some distinctive similarities and differences. First, we found the characteristic air-core penetration within the nozzle and the swirl chamber when the viscosity is lower, while it tends to disappear as the viscosity increases. Then, it is clearly visible that increasing the viscosity, also the breakup length increases, and the free liquid surface looks smooth and homogeneous along the hollow annular region. Finally, if we compare the Carreau fluid with the Newtonian fluid at low viscosity, we can see that the spray pattern looks almost identical, as in both cases the liquid viscosity is the same anywhere in the liquid sheet.

Compared to the limited viscosity variation observed in the power-law fluid in Figure 25a, a pronounced viscosity gradient is observed on the liquid-gas interface of a power-law fluid with a higher consistency index. The less shear thinning behaviour, the more the free-surface of the dispensing liquid experiences a wider range of higher viscosity.

This results in a different spray pattern as well as a different particle size distribution. In Figure 26, both shear rate and viscosity fields on an isosurface ($\alpha = 0.5$) of a power-law fluid with $k = 50 \text{ Pa} \cdot \text{s}^{-n}$ and $n = 0.27$ are shown. As supported by the previous VOF investigation, the injection of the power-law fluid with these rheological properties results in a conical sharp interface of the liquid film. However, compared to the non-Newtonian viscosity profiles computed through the VOF model in the previous section, the progressive mesh refinement implemented with the hybrid VOF-Lagrangian model enables a more accurate resolution of the viscosity field within the nozzle geometry.

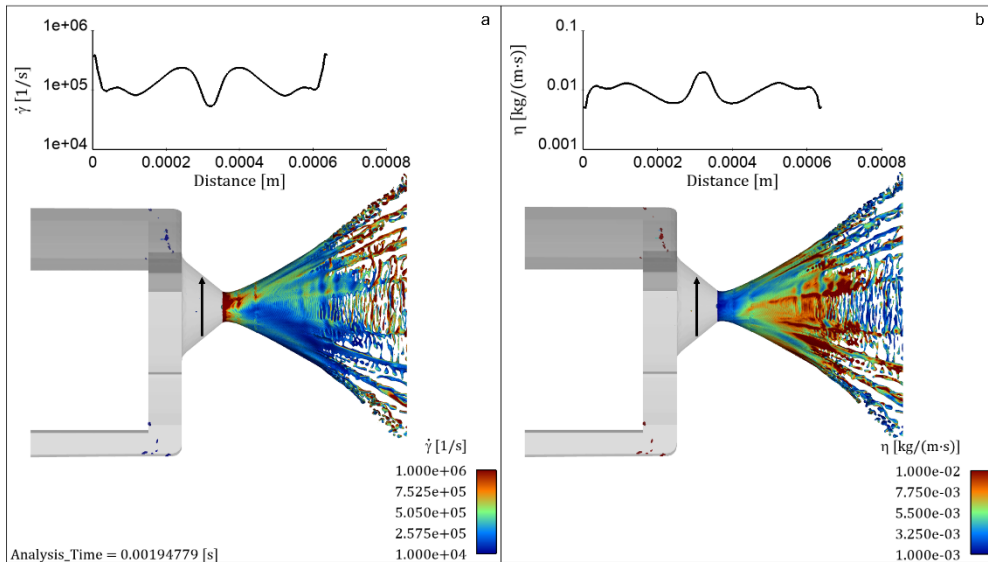


Figure 26 – Hollow-cone spray pattern of a non-Newtonian power-law fluid with $k = 50 \text{ Pa} \cdot \text{s}^{-n}$ and $n = 0.27$ with (a) shear rate profile at the middle of the spin chamber (top) and shear rate contour on the liquid-gas interface at $\alpha = 0.5$ (bottom), (b) viscosity profile at the middle of the spin chamber (top) and viscosity contour on the liquid-gas interface at $\alpha = 0.5$ (bottom).

In Figure 26a-26b, if we look at the shear rate and viscosity profiles at the middle of the nozzle conical end (spin chamber), it emerges that they are symmetric relative to the centre and specular in their shape.

The peculiar shape of those profiles is due to the characteristic transient air-core penetration that induces the swirling liquid to flow mainly at the middle region between the centre of the spin chamber and the nozzle wall. Due to the opposite effect of the liquid ejection through the annular region of the nozzle end with the air-core insertion along the axial direction, high velocity gradients occur in this region. The fluid elements in this annular region are, therefore, subjected to a higher deformation that, consequently, promotes the reduction of the viscosity. This phenomenon is reflected on the annular-shaped liquid sheet that emerges from the nozzle exit of the pressure-swirl device.

Furthermore, we observe a depicted increase of viscosity when the liquid-gas interface is no longer confined by the nozzle geometry, and a subsequent decrease of the viscous contracting force when the liquid lumps approach the aerodynamic breakup. The highest value of shear rate in the proximity of the nozzle exit involves, instead, a sudden drop of viscosity (Figure 26).

4.3 Particle Size Distribution (PSD) and spray pattern - Newtonian and non-Newtonian comparison

With the VOF-to-DPM model, in the previous section, we focused our attention on the primary breakup of the conical liquid sheet for Newtonian and non-Newtonian fluids. We investigated the influence of the key parameters on the ligament and droplet separation, without providing detailed information on the size distribution of the droplets produced by the primary atomization.

Concerning the discrete phase analysis, we compared different particle size distributions by varying with the liquid viscosity and the surface tension at fixed pressure injection, exit orifice diameter and liquid density. By including all the droplets detached from the hollow-cone liquid sheet at the final time of 2 ms, we examined four histograms that show the probability to find a droplet with a specific size in the outer extended domain (Figure 27). The droplet diameter ranges from around 10 to 150 μm .

In Figure 27, on one side, we observed that as the viscosity increases the droplet mean size slightly increases. This is due to the thickening of the hollow-cone liquid sheet that produces a broader range of larger ligaments and, consequently, bigger droplets.

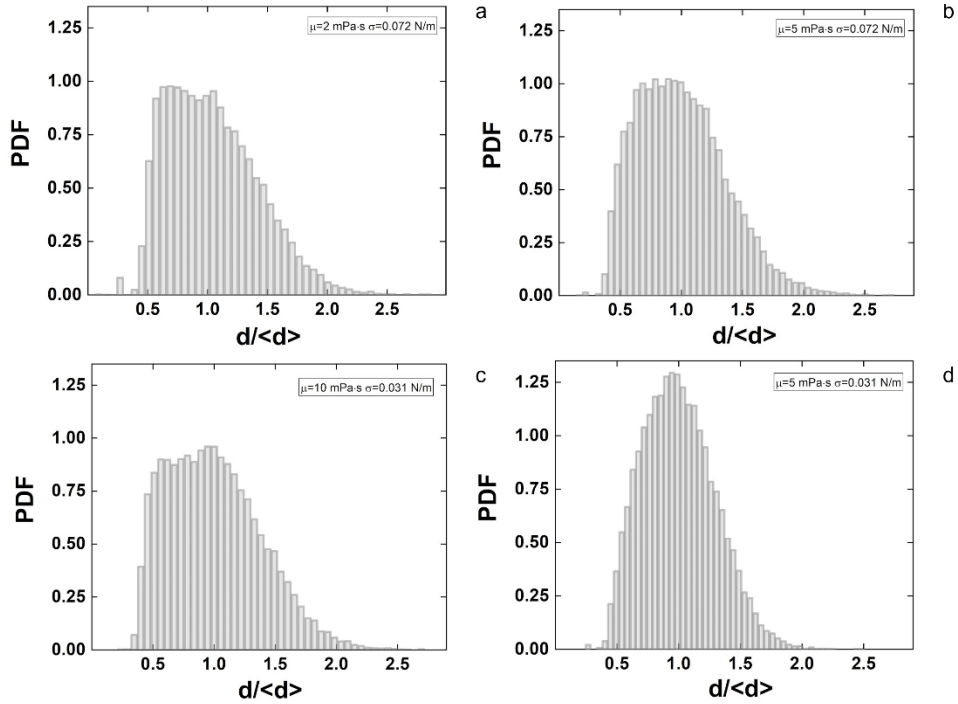


Figure 27 – Histograms of the droplets produced by the hollow-cone spray process up to $t = 2$ ms at $P_{inlet} = 4$ bar, $D_o = 0.32$ mm, and for (a) $\mu = 2$ mPa \cdot s, $\sigma = 0.072$ N/m, (b) $\mu = 5$ mPa \cdot s, $\sigma = 0.072$ N/m, (c) $\mu = 10$ mPa \cdot s, $\sigma = 0.072$ N/m, (d) $\mu = 5$ mPa \cdot s, $\sigma = 0.031$ N/m.

On the other side, if we keep fixed the viscosity, in this case 5 mPa \cdot s, but we halve the surface tension from 0.072 to 0.031 N/m, we can appreciate a significant decrease of the mean size complemented by a significant increase of total number of droplets tracked. As mentioned in the previous sections, this result can be explained by the reduction of the cohesive forces and, therefore, a resultant increase of the breakup frequency of the conical liquid sheet.

Keshavarz et al. (2016) observed that the final droplet size distribution of atomized Newtonian and non-Newtonian liquids is represented by a Gamma distribution, in which the Probability Density Function (PDF) is given by:

$$p\left(x = d/\langle d \rangle\right) = \Gamma(n, x) \equiv \frac{n^n}{(n-1)!} x^{n-1} e^{-nx} \quad (26)$$

where $\langle d \rangle$ is the mean droplet size. The scale factor n determines how narrow the distribution is and it is defined as:

$$n \equiv \frac{\langle d \rangle^2}{\langle d^2 \rangle - \langle d \rangle^2} \quad (27)$$

Large values of n indicate a narrow distribution and small values of n describe a broader distribution. Furthermore, the index n is a measure of the ligament corrugation which the final spray of droplets inherits in its size distribution.

In the hollow-cone spray process, the continuous breakup of the conical liquid sheet leads to reduce the annular liquid masses in ligaments and droplets. As the corrugation parameter increases, the more the hollow-cone ligaments produce small droplets. Indeed, by fitting the calculated particle size distribution with the Gamma distribution (Eq. (27)), it emerges that, according to Keshavarz et al. (2015), at $\sigma = 0.072$ N/m the corrugation factor is $n = 6$, while at the same operating condition and $\sigma = 0.031$ N/m, the hollow-cone spray produces smaller and homogeneous ligaments that increase n up to 10 (Figure 28).

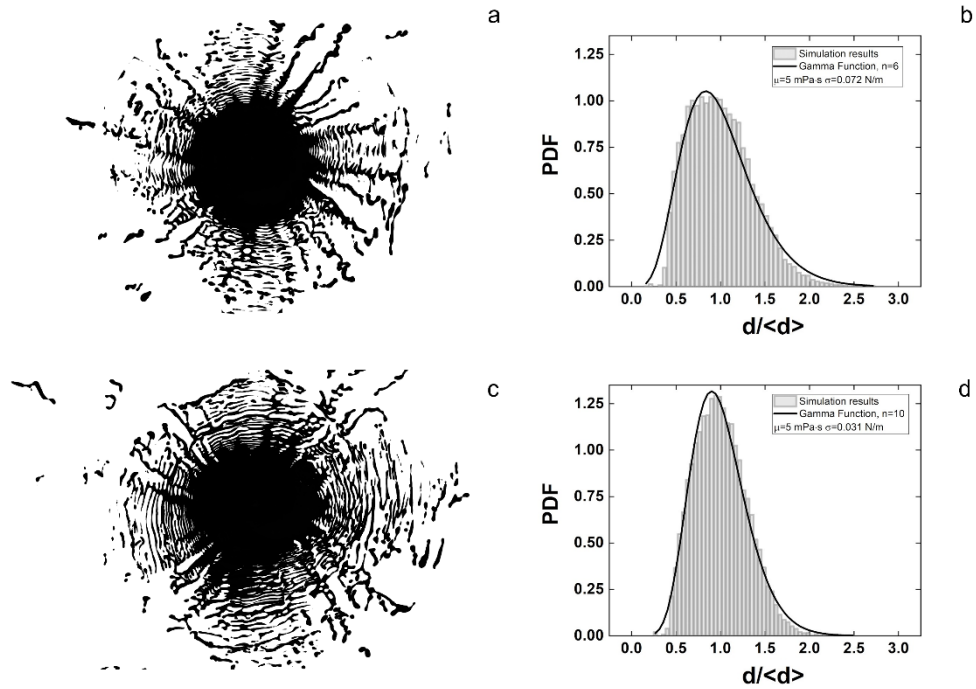


Figure 28 - (a) Liquid sheet disintegration features and (b) droplet size distribution with the corresponding gamma function fit ($n = 6$) of a Newtonian fluid at $\mu = 5 \text{ mPa} \cdot \text{s}$, $\sigma = 0.072 \text{ N/m}$. (c) Liquid sheet disintegration features and (b) droplet size distribution with the corresponding gamma function fit ($n = 10$) of a Newtonian fluid at $\mu = 5 \text{ mPa} \cdot \text{s}$, $\sigma = 0.031 \text{ N/m}$. The liquid-gas interface displacement and the particle distribution are taken at the final time of 2 ms with $P_{inlet} = 4 \text{ bar}$ and $D_o = 0.32 \text{ mm}$.

The significant increase of the corrugation factor at lower surface tension is directly correlated to the marked monodisperse distribution of droplets that we observed in Figure 27d. During the fragmentation of the conical film in small liquid structures, the hollow-cone spray at $\sigma = 0.031 \text{ N/m}$ produces smoother ligaments with a reduced breakup time/length. Compared to the fluid at $\sigma = 0.072 \text{ N/m}$, the liquid lump quickly breaks up into uniform ligaments, preventing from local fluctuations at the liquid-gas interface that would broaden the final droplet size distribution (Figure 28).

By adopting the same operating conditions in terms of pressure injection and geometric parameters, we investigate on the gamma distribution of different power-law fluids. As in the case of the Newtonian liquids, the gamma function well matches the particle size distribution we got from the numerical simulations of the non-Newtonian spray at the final time of 2 ms. In Figure 29, we show three different gamma distributions of power-law fluids, in which we change either the consistency index or the surface tension. For $k = 50 \text{ Pa} \cdot \text{s}^{-n}$, $n = 0.27$ and $\sigma = 0.072 \text{ N/m}$, the droplet size distribution exhibits the same corrugation factor of a Newtonian fluid at $5 - 10 \text{ mPa} \cdot \text{s}$. As observed for the surface tension sweep of the Newtonian fluid, the decrease of this property leads to increase n . In this case, however, the corrugation factor undergoes a slighter increase from 6 to 8, instead of 10 (Figure 28-29). The corresponding broadened distribution at the same low surface tension may be related to the viscosity gradient that affects the ligament shape during the primary breakup, resulting in a more polydisperse spray. If we, instead, reduce k from $50 \text{ Pa} \cdot \text{s}^{-n}$ to $10 \text{ Pa} \cdot \text{s}^{-n}$, we observe a marked increase of n that is due to the significant reduction of viscosity that the liquid flow experiences at the shear rate range of interest (see Figure 26, section 4.2.1).

Regardless of the Newtonian or non-Newtonian behavior of the liquid dispensed, the computed particle size distribution of the spray process is accurately predicted by using a Gamma function with an appropriate scale factor n , as supported by Keshavarz et al. (2015).

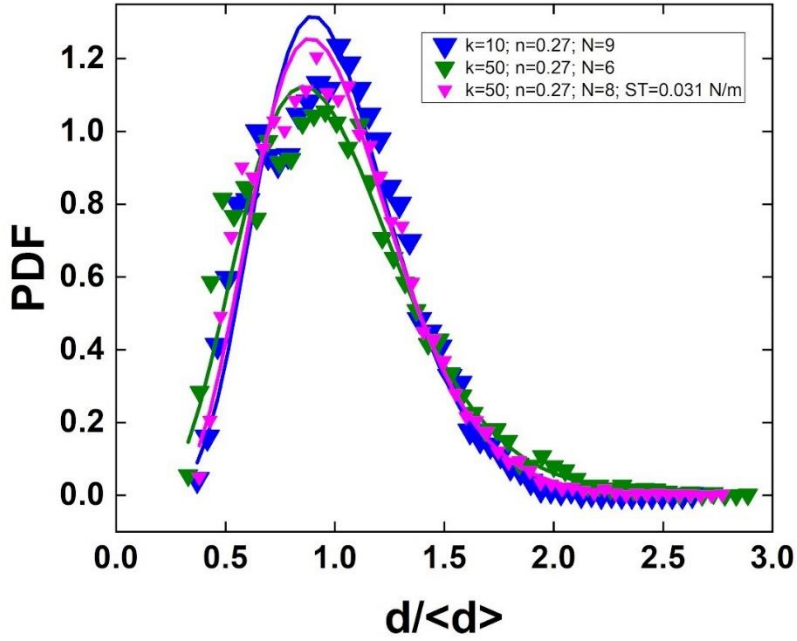


Figure 29 – Gamma distribution function of droplets produced by the hollow-cone atomization process of power-law fluids with $k = 10 \text{ Pa} \cdot \text{s}^{-n}$, $n = 0.27$, $\sigma = 0.072 \text{ Nm}^{-1}$ (in blue), $k = 50 \text{ Pa} \cdot \text{s}^{-n}$, $n = 0.27$, $\sigma = 0.072 \text{ Nm}^{-1}$ (in green), $k = 50 \text{ Pa} \cdot \text{s}^{-n}$, $n = 0.27$, $\sigma = 0.031 \text{ Nm}^{-1}$ (in magenta).

If we compare the Newtonian and non-Newtonian spray pattern and particle propagation, we can observe that the dynamics of the liquid sheet breakup is significantly different, and it can affect the spray performance. In Figure 30, we show the distinctive hollow-cone spray evolution of the power-law fluid at $k = 50 \text{ Pa} \cdot \text{s}^{-n}$ and $n = 0.27$, compared with the Newtonian fluid at $\eta = 10 \text{ mPa} \cdot \text{s}$. At $t \sim 1 \text{ ms}$, the initial atomization process of the two fluids is described by dissimilar liquid sheet morphology and droplet spreading direction. The shear-thinning behavior of the power-law spray induces a drop of viscosity in proximity of the nozzle exit, where the releasing liquid is strongly perturbed by higher shear rate (see Figure 26, section 4.2.1). As the

annular liquid sheet flows out from the exit orifice, the progressive decrease of viscosity promotes the air-core penetration up to the rear of the swirl chamber. The transient inception of the air pushes the thin liquid sheet towards the wall, promotes its rotating motion within the spin chamber and, consequently, delays the liquid expulsion. The induced rotating motion within the swirl chamber persists once the liquid sheet emerges from the nozzle. As a result, the tiny droplets produced at the beginning of the liquid film disruption will spread in radial direction and remain suspended surrounding the nozzle (Figure 30a-30c). At $t = 2$ ms, the air penetration within the nozzle is vanished in response to the liquid flow at higher viscosity towards the centre of the spin chamber (see Figure 26, section 4.2.1).

Conversely, the fluid dynamics of the Newtonian atomization process results in a sharp and extended hollow-cone interface from the first moments of the liquid ejection. Therefore, the hollow-cone shape of the atomized Newtonian fluid stabilizes rapidly relative to the non-Newtonian power-law fluid. The ligaments and the droplets detach from the main liquid body exclusively following the streamwise direction provided by the stable conical liquid sheet (Figure 30b-30d). We observed, moreover, that the more pronounced shear-thinning behavior (i.e., increase of k and/or decrease of n), the higher is the number of suspended particles surrounding the nozzle region. For Newtonian fluid at lower viscosity ($\eta \sim 1$ mPa \cdot s), instead, this phenomenon still occurs, but it is less marked, with least amount of satellite droplets and different spray pattern.

From an applicative point of view, the fluctuations of droplets outside the hollow-cone spray region may strongly worsen the performance of the pressure-swirl devices.

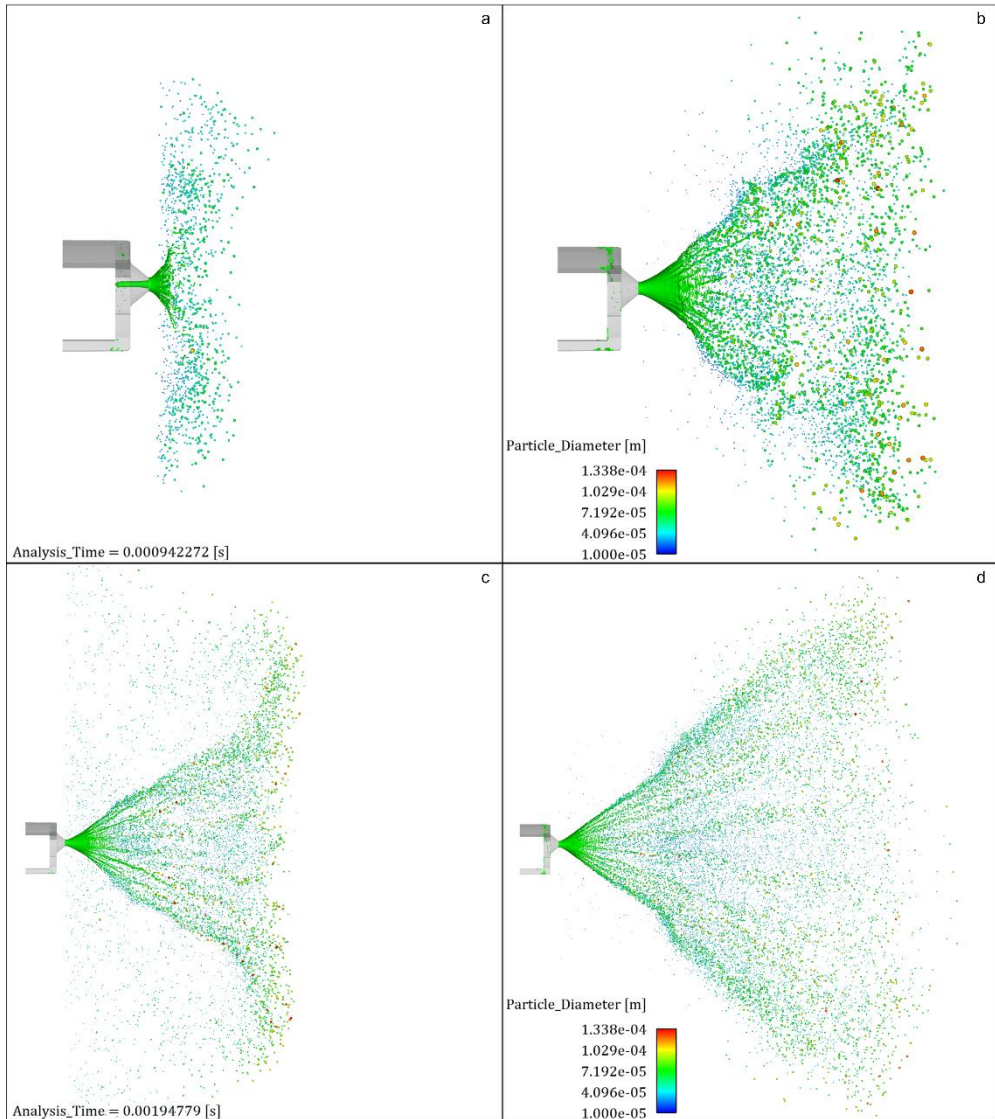


Figure 30 – Comparison of Newtonian and non-Newtonian spray pattern and droplet displacement at different dispensing time. At $t = 1$ ms, hollow-cone spray atomization of (a) power-law fluid with $k = 50 \text{ Pa} \cdot \text{s}^{-n}$ and $n = 0.27$ and (b) Newtonian fluid with $\mu = 10 \text{ mPa} \cdot \text{s}$. Hollow-cone spray atomization of (c) power-law fluid with $k = 50 \text{ Pa} \cdot \text{s}^{-n}$ and $n = 0.27$ and (d) Newtonian fluid with $\mu = 10 \text{ mPa} \cdot \text{s}$ at $t = 2$ ms.

5. Conclusion

The present CFD study describes all the key aspects of the hollow-cone atomization produced by a simplex pressure-swirl atomizer. With the VOF method, we carried out several transient simulations in which the liquid-gas interactions are solved both within and outside the nozzle, simultaneously. With a static grid discretization, we initially track and detect the liquid-gas interface displacement only within the nozzle and at small distance from the exit orifice. Depending on different liquid properties and geometric features, we examined qualitatively and quantitatively the hollow-cone spray performance in terms of cone angle and liquid sheet morphology. We assessed the spray

performance in terms of liquid sheet thickness, cone angle and jet length at different operating pressures.

For a Newtonian fluid, by properly tuning Reynolds and Ohnesorge numbers, we showed that it is possible to differentiate two main spray configurations: spraying and jetting. The classical hollow-cone shape resulting from a pressure-swirl atomizer can degenerate into a straight jet under specific operating conditions. When the conical film collapses in on itself, the resulting spray deteriorates in terms of ligament and drop formation. We find out that stable hollow-cone sprays are observed if a critical Reynolds number (around 600) is overcome. To our knowledge, this is the first time such a stability criterion is proposed.

Then, we extended the study by considering the droplets detachment at a larger distance from the nozzle exit orifice. This step required the implementation of the VOF-to-DPM model and a switch of the mesh refinement technique from static to dynamic. In this way, we make possible to get consistent numerical results by discretizing a larger domain with a reasonable number of cells. The modeling and simulation of the film disintegration dynamics allowed us to verify the consistency of the stability criterion of the hollow-cone spray also at larger distance from the nozzle. In this regard, we observed the effects of the hollow-cone destabilization in terms of ligaments/droplets propagation together with their impact against a wall located at 5 cm of distance from the nozzle outlet. Nozzle design and fluid properties do affect the hollow-cone primary atomization and the spray pattern

produced by the droplets that cover the rigid surface placed far from the pressure-swirl device.

Since the significance of the viscosity effect is widely acknowledged in the field of pressure-swirl atomizers, we focused our attention also on the atomization quality by comparing the Newtonian and non-Newtonian fluid behaviors. In both cases, we found a critical viscosity of approximately $10 \text{ mPa} \cdot \text{s}$ that marks the switch from spraying to jetting regime for specific operating conditions.

Moreover, we stressed the importance of the non-Newtonian liquid properties. By increasing the consistency and the shear thinning indexes, we show that the liquid sheet shape/size, the breakup time/length, and the resultant droplet distribution can significantly change. From this perspective, we succeeded in extending the non-Newtonian behaviors not only for the liquid sheet morphology but also for the ligaments and the droplets generated downstream of the primary atomization. To our knowledge, this is the first time that a detailed three-dimensional computational study of the non-Newtonian hollow-cone primary atomization is proposed. By comparing the fluid dynamics of Newtonian/non-Newtonian hollow-cone sprays emerged that the viscous shear-rate dependence of a power-law fluid can promote the formation of tiny droplets suspended all around the nozzle, under specific operating conditions. This aspect turns out to be crucial in spray applications where the key objective is to optimize the spray performance.

Moreover, we deeply investigated the effects of the various primary breakup scenarios on the particle size distribution (PSD). According to

the literature, we observed that the probability density function that better predicts the droplet size distribution is the Gamma function with a specific value of the scale factor n for Newtonian and non-Newtonian fluids. Regardless of the rheological behaviour of the fluids, we found out that viscosity and surface tension may strongly affect the corrugation factor n with a resultant improvement or worsening of the atomization quality in terms of particle size distribution.

For what it concerns the future perspective, from the CFD modeling and simulation point of view, it would be interesting to include to this code other relevant atomization phenomena such as coalescence, secondary breakup, and evaporation. This study focused the attention only on the non-Newtonian viscous effects, while further developments in the field of spray applications would require the implementation of the viscoelastic fluid properties.

In conclusion, a detailed experimental study of this small-scale hollow-cone spray at the operating condition adopted in this work would allow to better validate the numerical results.

We hope that our research work will be of interest in the product design to predict and determine the more appropriate operating parameters, improving the hollow-cone spray performance.

Acknowledgments

I would like to thank *Prof. Pier Luca Maffettone* and *Ph.D. Deepak Ahirwal* for giving me the opportunity to take part of this exciting and challenging research work. Over the years, they always supported and encouraged me to improve the quality of this research activity.

Additionally, discussions and collaborations with my research group "*Bottega della Materia Soffice*" and *P&G community* have been significant to enrich my research experience during these three years. Thank you all.

I want to dedicate this work to *my family* and *friends* that greatly supported me every day. Without them, this experience would not have been the same.

References

Amini, G., "Liquid flow in a simplex swirl nozzle". International Journal of Multiphase Flow. Volume 79, 225-235 (2016).

Anufriev, I.S., Shadrin, E.Y., Kopyev, E.P., Sharypov, O.V., Leschevich, V.V., "Liquid Fuel spraying by high-speed steam jet". Thermophysics and Aeromechanics. Volume 27, 627-630 (2020).

Bianchi, G.M., Minelli, F., Scardovelli, R., Zaleski, S., "3D Large Scale Simulation of the High-Speed Liquid Jet Atomization". SAE Transactions, Journal of Engines. Volume 116, 333-346 (2007).

Billant, P., Chomaz, J.M., Huerre P., "Experimental study of vortex breakdown in swirling jets". *Journal of Fluid Mechanics*. Volume 376, 183-219 (1998).

Brackbill, J.U., Kothe, D.B., Zemach, C., "A continuum method for modeling surface tension". *Journal of Computational Physics*. Volume 100, Issue 2, 335-354 (1992).

Cadnum, J.L., Jencson, A.L., Livingston, S.H., Li, D.F., Redmond, S.N., Pearlmutter, B., Wilson, B.M., Donskey, C.J., "Evaluation of an electrostatic spray disinfectant technology for rapid decontamination of portable equipment and large open areas in the era of SARS-CoV-2". *American Journal of Infection Control*. Volume 48, 951-954 (2020).

Davanlou, A., Basu, S., Lee, J., Kumar, R., "THE EFFECTS OF SURFACTANT ON SIMPLEX NOZZLE SPRAY BEHAVIOR AND ITS COMPARISON TO LIQUID FUELS ", *Proceedings of the ASME 2013 International Mechanical Engineering Congress* (2013).

De Padova, D., Mossa, M., "Multi-phase simulation of infected respiratory cloud transmission in air". *AIP Advances*, 11, 035035 (2021).

Desjardins, O., Moureau, V., Pitsch, H., "An accurate conservative level set/ghost fluid method for simulating turbulent atomization". *Journal of Computational Physics*. Volume 227, Issue 18, 8395-8416 (2008).

De Villiers, E., Gosman, A.D., Weller, H.G., "Large Eddy Simulation of Primary Diesel Spray Atomization". SAE Transactions, Journal of Engines. Volume 113, 193-206 (2004).

Ding, J.-W., Li, G.-X., Yu, Y.-S., Li, H.-M., "Numerical investigation on primary atomization mechanism of hollow cone swirling sprays". International Journal of Rotating Machinery. Volume 2016, 1201497 (2016).

Douglas, C.M., Emerson, B.L., Lieuwen, T.C., "Nonlinear dynamics of fully developed swirling jets". Journal of Fluid Mechanics. Volume 924, A14 (2021).

Dumouchel, C., "On the experimental investigation on primary atomization". Exp Fluids (2008).

Feng, Y., Marchal, T., Sperry, T., Yi, H., "Influence of wind and relative humidity on the social distancing effectiveness to prevent COVID-19 airborne transmission: A numerical study". Journal of Aerosol Science. Volume 147, 105585 (2020).

Fuster, D., Bague, A., Boeck, T., Le Moyne, L., Leboissetier, A., Popinet, S., Ray, P., Scardovelli, R., Zaleski, S., "Simulation of primary atomization with an octree adaptive mesh refinement and VOF method". International Journal of Multiphase Flow. Volume 35, Issue 6, 550-565 (2009).

Gorokhovski, M., Herrmann, M., "Modeling Primary Atomization. Annual Review of Fluid Mechanics". Vol. 40: 343-366 (2008).

Gosman, A. D., Ioannides, E., "Aspects of computer simulation of liquid-fuelled combustors". J. Energy. 7(6). 482-490 (1983).

Harlow, F.H., Welch, J.E., "Numerical Study of Large-Amplitude Free-Surface Motions". Physics of Fluids. Volume 9, Issue 5, 842 (1966).

Hirt, C.W., Nichols, B.D., "Volume of fluid (VOF) method for the dynamics of free boundaries". Journal of Computational Physics. Volume 39, Issue 1, 201-225 (1981).

Jeon, S., Kim, S., Park, G., "Numerical study of condensing bubble in subcooled boiling flow using volume of fluid model". Chemical Engineering Science. Volume 66, 5899-5909 (2011)

Keshavarz, B., Sharma, V., Houze, E.C., Koerner, M.R., Moore, J.R., Cotts, P.M., Threlfall-Holmes, P., McKinley, G.H., "Studying the effects of elongational properties on atomization of weakly viscoelastic solutions using Rayleigh Ohnesorge Jetting Extensional Rheometry (ROJER)". Journal of Non-Newtonian Fluid Mechanics. Volume 222, 171-189 (2015).

Keshavarz, B., Houze, E.C., Moore, J.R., Koerner, M.R., McKinley, G.H., "Ligament mediated fragmentation of Viscoelastic liquids". *Physical Review Letters*, 117 (2016)

Kuznetsov, V., Shebelev, A., Sharypov, O., Dekterev, A., Minakov, A., "Simulation of the liquid fuel spraying based on Eulerian-Lagrangian model". *Journal of Physics: Conference Series*, 1359 (2019).

Laurila, E., Roenby, J., Maakala, V., Peltonen, P., Kahila, H., Vuorinen, V., "Analysis of viscous fluid flow in a pressure-swirl atomizer using large-eddy simulation". *International Journal of Multiphase Flow*. Volume 113, 371-388 (2019).

Laurila, E., Koivisto, S., Kankkunen A., Saari, K., Maakala, V., Jarvinen M., Vuorinen, V., "Computational and experimental investigation of a swirl nozzle for viscous fluids". *International Journal of Multiphase Flow*. Volume 128, 103278 (2020).

Lee, Z., Kimb, T., Park, Sun., Park, Suh., "Review on spray, combustion, and emission characteristics of recent developed direct-injection spark ignition (DISI) engine system with multi-hole type injector". *Fuel*. Volume 259, 116209 (2020).

Lefebvre, A.H., McDonell, V.G., "Atomization and Sprays". CRC Press, Taylor & Francis Group (2017).

Li, X., Soteriou, M., "High-fidelity simulation of fuel atomization in a realistic swirling flow injector". *Atomization and Sprays*. Volume 23, Issue 11, 1049-1078 (2013).

Li, X., Soteriou, M., "High-fidelity simulation and analysis of liquid jet atomization in a gaseous crossflow at intermediate Weber numbers". *Physics of Fluids*. Volume 28, 082101 (2016).

Lilley, D.G., "Prediction of Inert Turbulent Swirl Flows". *AIAA Journal*. Volume 11, 7 (1973).

Lippert, A.M., Chang, S., Are, S., Schmidt, D.P., "Mesh Independence and Adaptive Mesh Refinement for Advanced Engine Spray Simulations". *SAE Technical Paper* (2005).

Madlener, K., Frey, B., Ciezki, H. K., "GENERALIZED REYNOLDS NUMBER FOR NON-NEWTONIAN FLUIDS", *Progress in Propulsion Physics* 1 237-250 (2009).

Maly, M., Jedelsky, J., Slama, J., Janackova, L., Sapik, M., Wigley, G., Jicha, M., "Internal flow and air core dynamics in Simplex and Spill-return pressure-swirl atomizers". *International Journal of Heat and Mass Transfer*. Volume 123, 805-814 (2018).

Menard, T., Tanguy, S., Berlemont, A., "Coupling level set/VOF/ghost fluid methods: Validation and application to 3D simulation of the

primary break-up of a liquid jet". *International Journal of Multiphase Flow*. Volume 33, Issue 5, 510-524 (2007).

Mirjalili, S., Jain, S.S., Dodd, M.S., "Interface-capturing methods for two-phase flows: An overview and recent developments". *Center for Turbulent Research. Annual Research Briefs* (2017)

Morris, C.E., O'Doherty, D.M., Mason-Jones, A., O'Doherty, T., "Evaluation of the swirl characteristics of a tidal stream turbine wake". *International Journal of Marine Energy*. Volume 14, 198-214 (2016).

Morsi, S. A., Alexander, A. J., "An Investigation of Particle Trajectories in Two-Phase Flow Systems". *J. Fluid Mech.* 55(2). 193–208 (1972).

Ohnesorge, W., "The formation of drops by nozzles and the breakup of liquid". *Journal of Applied Mathematics and Mechanics*. Vol. 16, 355 (1936).

Osher, S., Fedkiw, R.P., "Level Set Methods: An Overview and Some Recent Results". *Journal of Computational Physics*. Volume 169, Issue 2, 463-502 (2001).

Ozkan, F., Worner, M., Wenka, A., Soyhan, H.S., "Critical evaluation of CFD codes for interfacial simulation of bubble-train flow in a narrow channel". *International Journal For Numerical Methods In Fluids*. Volume 55, 537-564 (2007).

Pendar, M.-R., Pascoa, J.C., "Numerical analysis of charged droplets size distribution in the electrostatic coating process: Effect of different operational conditions". *Physics of Fluids*. Volume 33, Issue 3, 033317 (2021).

Prakash, R.S., Gadgil, H., Raghunandan, B.N., "Breakup processes of pressure swirl spray in gaseous cross-flow". *International Journal of Multiphase Flow*. Volume 66, 79-91 (2014).

Rajamanickam, K., Basu, S., "On the dynamics of vortex-droplet interactions, dispersion and breakup in a coaxial swirling flow". *J. Fluid Mech*. Volume 827, 572-613 (2017).

Rayleigh, L., "On the instability of jets". *Proceedings of the London Mathematics Society*. S1-S10 (1), 4-13 (1878).

Rezaeimoghaddam, M., Elahi, R., Razavi, M.R.M., Ayani, M.B., "Modeling of non-Newtonian fluid flow within simplex atomizers". *Proceedings of the ASME 2010 10th Biennial Conference on Engineering Systems Design and Analysis*. ESDA2010-25266 (2010).

Rizk, N.K., Lefebvre, A.H., "Internal Flow Characteristics of Simplex Swirl Atomizers". *J. Propulsion*. Volume 1, 3 (1985).

Rizk, N.K., Lefebvre, A.H., "Prediction of Velocity Coefficient and Spray Cone Angle for Simplex Swirl Atomizers". International Journal of Turbo and Jet-Engines. Volume 4, 65-73 (1987).

Rocha, A.D, Bannwart, A.C., Ganzarolli, M.M., 2015. Numerical and experimental study of an axially induced swirling pipe flow. International Journal of Heat and Fluid Flow. Volume 53, 81-90.

Saha, A., Lee, J.D., Basu, S., Kumar, R., "Breakup and coalescence characteristics of a hollow-cone swirling spray". Physics of Fluids. Volume 24, Issue 12, 124103 (2012).

Sallam, K.A., Dai, Z., Faeth, G.M., "Liquid breakup at the surface of turbulent round liquid jets in still gases". International Journal of Multiphase Flow. Volume 28, Issue 3, 427-449 (2002).

Seminara, G., Carli, B., Forni, G., Fuzzi, S., Mazzino, A., Rinaldo, A., "Biological fluid dynamics of airborne COVID-19 infection". Rendiconti Lincei, Scienze Fisiche e Naturali. Volume 31, 505-537 (2020).

Shao, C., Luo, K., Yang, Y., Fan, J., "Detailed numerical simulation of swirling primary atomization using a mass conservative level set method". International Journal of Multiphase Flow. Volume 89, 57-68 (2017).

Shao, C., Luo, K., Chai, M., Fan, J., "Sheet, ligaments and droplet formation in swirling primary atomization". AIP Advances. Volume 8, Issue 4 (2018).

Shavit, U., Chigier, N., "The role of the dynamic surface tension in air assist atomization". Physics of Fluids 7, 24 (1995).

Shi, H., Kleinstreuer, C., "Simulation and Analysis of High-Speed Droplet Spray Dynamics". Journal of Fluids Engineering. 129 (5), 621-633 (2007).

Shim, Y.-S., Choi, G.-M., Kim, D.-J., "Numerical and experimental study on hollow-cone fuel spray of high-pressure swirl injector under high ambient pressure condition". Journal of Mechanical Science and Technology. Volume 22, 320-329 (2008).

Shinjo, J., Umemura, A., "Simulation of liquid jet primary breakup: Dynamics of ligament and droplet formation". International Journal of Multiphase Flow. Volume 36, 513-532 (2010).

Singh, G., Kourmatzis, A., Gutteridge, A., Masri, A.R., "Instability growth and fragment formation in air assisted atomization". Journal of Fluid Mechanics. Volume 892, A29 (2020)

Sinha, A., Prakash, R. S., Mohana, A.M., Ravikrishna, R.V., "Airblast spray in crossflow - Structure, trajectory and droplet sizing". *International Journal of Multiphase Flow*. Volume 72, 97-111 (2015).

Sirignano, W.A., Mehring, C., "Review of theory of distortion and disintegration of liquid streams". *Progress in Energy and Combustion Science*. Volume 26 Issues 4-6, 609-655 (2000).

Sivakumar, D., Raghunandan, B. N., "Converging swirling liquid jets from pressure swirl atomizers: Effect of inner air pressure". *Physics of Fluids*. Volume 14, 4389 (2002).

Som, S.K., "Air core in pressure swirl atomizing nozzles". *Atomization and Sprays*. Volume 22, Issue 4, 283-303 (2012).

Tonini, S., Gavaises, M., Theodorakakos, A., "Modelling of high-pressure dense diesel sprays with adaptive local grid refinement". *International Journal of Heat and Fluid Flow*. Volume 29, Issue 2, 427-448 (2008).

Vegad, C.S., Kumar, A., Chakravarthy, S.R., "Dynamics of free-surface mutually perpendicular twin liquid sheets and their atomization characteristics". *Physics of Fluids*. Volume 31, Issue 8, 082103 (2019).

Wu, H., Zhang, F., Zhang, Z., “Droplet breakup and coalescence of an internal-mixing twin-fluid spray”. *Physics of Fluids*. Volume 33, Issue 1, 013317 (2021).

Yao, S., Zhang, J., Fang, T., “Effect of viscosities on structure and instability of sprays from a swirl atomizer”. *Experimental Thermal and Fluid Science*. Volume 39, 158-166 (2012).

Yujie, Z., Mingyan, L., Yonggui, X., Can, T., “Three-dimensional volume of fluid simulations on bubble formation and dynamics in bubble columns”. *Chemical Engineering Science*. Volume 73, 55-78 (2012)

Zahedi, P., Saleh, R., Moreno-Atanasio, R., Yousefi, K., “Influence of fluid properties on bubble formation, detachment, rising and collapse; Investigation using volume of fluid method”. *Korean J. Chem. Eng.*, 31(8), 1349-1361 (2014).

Zhao, J., Tong, Y., Ren, Y., Zhu, Y., Chen, Z., Lin, W., Nie, W., “Structures of liquid jets in supersonic crossflows in a rectangular channel with an expansion section”. *Physics of Fluids*. Volume 32, Issue 11, 111704 (2020).

Zhao, Y., Tan, H.H., Zhang, B., “A High-Resolution Characteristics-Based Implicit Dual Time-Stepping VOF Method for Free Surface Flow

Simulation on Unstructured Grids". Journal of Computational Physics.
Volume 183, Issue 1, 233-273 (2002).